Available online at www.sciencedirect.com
ScienceDirect
Journal of Computational Physics 227 (2008) 7322–7345
JOURNAL OF COMPUTATIONAL PHYSICS
www.elsevier.com/locate/jcp

Lacunae based stabilization of PMLs

H. Qasimov, S. Tsynkov *

Department of Mathematics, North Carolina State University, P.O. Box 8205, Raleigh, NC 27695, USA

Received 6 June 2007; received in revised form 15 April 2008; accepted 17 April 2008
Available online 30 April 2008

Abstract

Perfectly matched layers (PMLs) are used for the numerical solution of wave propagation problems on unbounded regions. They surround the finite computational domain (obtained by truncation) and are designed to attenuate and completely absorb all the outgoing waves while producing no reflections from the interface between the domain and the layer. PMLs have demonstrated excellent performance for many applications. However, they have also been found prone to instabilities that manifest themselves when the simulation time is long. Hereafter, we propose a modification that stabilizes any PML applied to a hyperbolic partial differential equation/system that satisfies the Huygens' principle (such as the 3D d'Alembert equation or Maxwell's equations in vacuum). The modification makes use of the presence of lacunae in the corresponding solutions and allows us to establish a temporally uniform error bound for arbitrarily long-time intervals. At the same time, it does not change the original PML equations. Hence, the matching properties of the layer, as well as any other properties deemed important, are fully preserved. We also emphasize that besides the aforementioned PML instabilities per se, the methodology can be used to cure any other undesirable long-term computational phenomenon, such as the accuracy loss of low order absorbing boundary conditions.

Keywords: Perfectly matched layer (PML); Long-time stability; Weak well-posedness; Wave propagation; Hyperbolicity; The Huygens' principle; Lacunae; Maxwell's equations; Artificial boundary conditions (ABCs); Numerical solution

1. Introduction

Numerical solution of infinite-domain problems requires truncation of the unbounded domain for the purpose of constructing a finite-dimensional discretization. In doing so, one clearly needs to set some artificial boundary conditions (ABCs) at the outer boundary of the finite computational domain [1,2]. The ABCs shall provide a closure for the truncated formulation and guarantee that its solution will not differ much from the corresponding fragment of the original infinite-domain solution (ideally, will coincide with it).

For the problems of propagation of electromagnetic waves, a very efficient closure mechanism was introduced by Bérenger [3,4]. He proposed to surround the computational domain by a layer of artificial material

* Corresponding author.
E-mail addresses: hrqasimo@ncsu.edu (H. Qasimov), tsynkov@math.ncsu.edu (S. Tsynkov).
URL: http://www.math.ncsu.edu/~stsynkov (S. Tsynkov).

0021-9991/$ - see front matter © 2008 Elsevier Inc. All rights reserved.
doi:10.1016/j.jcp.2008.04.018

capable of rapidly damping all the outgoing waves while generating no reflections from the interface between the domain and the layer, regardless of the wave's frequency or angle of incidence. It was called a perfectly matched layer (PML). The PML capabilities were attained in work [3,4] by splitting the field components, i.e., introducing additional unknowns and equations in the layer, and then using the resulting extra degrees of freedom for the development of an efficient waves' attenuation strategy. Subsequently, similar techniques were proposed for other wave propagation problems, such as acoustics [5] and elasticity. Note that the PML never alters the propagation speed as it would immediately create a scattering mechanism for the waves, it only reduces their amplitude.

It has also been noticed [6], however, that the Bérenger's split transforms the strongly hyperbolic (symmetric) Maxwell's equations into a weakly hyperbolic system, which, in turn, implies transition from strong well-posedness to weak well-posedness of the Cauchy problem [7].[1] A weakly well-posed system can become ill-posed under a low order perturbation, and an example of such a perturbation for the Bérenger's equations was given in [6]. Even though it has later been shown [9] that the actual form of the Bérenger's system does not lead to ill-posedness, the system still remains only weakly well-posed, *and a linear growth of the split field components inside the PML is possible*. This behavior may also lead to a purely numerical instability of the discretization. In particular, it has been proved in [6] that the very popular Yee scheme [10] becomes unconditionally unstable in the PML [3,4], with the powers of the amplification matrices growing linearly as the number of time steps increases.

From the standpoint of applications, the split field PML of [3,4] has demonstrated an overall excellent performance. However, concerns about its well-posedness and stability have prompted the development of other types of PMLs for computational electromagnetism [11–13] and other areas (e.g., acoustics [14]). These alternative strategies do not require splitting the field components in the PML, although they still introduce additional unknowns inside the layer. Later, however, *the unsplit PMLs have also been found susceptible to gradually developing instabilities [15]*. They have first been predicted theoretically and then *corroborated by the actual computations*, e.g., for the two-dimensional TE polarized Maxwell's equations [15]. A systematic experimental study of the long-time performance of unsplit PMLs with several commonly used explicit second order schemes has been conducted in our recent paper [16].

Note that if some components of the solution begin to grow inside the PML, the resulting numerical artifacts from the layer may or may not contaminate the computational domain, depending on the particular application and the design of the scheme. As mentioned, e.g., in [17], the Yee scheme can keep the instability inside the layer, whereas a higher order scheme of [15] propagates it back to the domain. As, however, has been noticed in [18], for the reason of improving the numerical performance on parallel platforms, a code that includes a split field PML is often designed in such a way that the equations solved inside the domain (not in the layer) are also split, although with no damping factors. In this case, even the Yee scheme appears capable of allowing the contamination from the layer into the domain.

An approach has been proposed in [15] to cure the long-time instability of unsplit PMLs. This approach is based on changing the governing equations in the layer. It has been experimentally shown to work well, but theoretically it is unclear whether the modified layer remains perfectly matched and absorbing.

Other remedies can also be found in the literature. For example, the non-linear PML of [19] guarantees boundedness of the energy integrals and strong well-posedness of the governing equations in the layer. However, its practical implementation requires a certain regularization to keep the denominators away from zero. Again, computationally it has been shown to perform well, but the analysis does not extend to this case. The complex frequency-shifted PML introduced in [20,21] and analyzed in detail in [17] also guarantees boundedness of the energy integrals and strong well-posedness.[2] However, the frequency shift in the PML leads to the loss of frequency independent absorption [17].

Altogether, the aforementioned stabilizing changes inside the PML often show no detrimental effect of any kind in the experiments, even when the supporting analysis is lacking. Moreover, according to a number of authors (see, e.g., [8]), the long-time instability of the PMLs may only have a limited negative effect in practical

[1] In fact, weak well-posedness characterizes all split field PMLs, see, e.g., [8].
[2] For the analysis of well-posedness see also [22].

computations, in particular, because often by the time it manifests itself the phase errors would have already killed the solution [18]. We tend to believe, however, that the deterioration of solution due to the phase errors is not always that rapid (Section 3), and as any potentially adverse phenomenon, the long-term instability of the PMLs needs to be carefully addressed.

Therefore, *the key objective of the current paper is to introduce a cure for the long-time instability of the PMLs while keeping all the advantageous properties of a given layer unaffected (such as matching, absorption, etc.)*. At least as important, the proposed cure has to be fully and rigorously justified. To achieve this objective, we employ the lacunae-based integration. We should additionally note that even though the lacunae-based integration is presented hereafter as an approach to mitigating the long-time instability of the PMLs, the analysis of Section 2 clearly indicates that *it can also be used for alleviating any other undesirable long-time phenomenon in computation*, e.g., the deterioration of accuracy of low order local ABCs.

Lacunae-based methods for the numerical integration of hyperbolic equations and systems have been developed during the past several years. They apply to the equations that satisfy the Huygens' principle [23–28]. For the problem of radiation of waves by a known source, they guarantee a temporally uniform grid convergence for any consistent and stable scheme [29]. The basic idea of lacunae-based methods is that once the domain of interest falls completely into the lacuna of the solution [30], the integration does not need to be continued any further. The presence of lacunae can also be efficiently exploited for the construction of exact ABCs[3] for various wave propagation problems [31–33]. These ABCs have only fixed and limited extent of temporal non-locality.

Hereafter, we apply the concepts of lacunae-based integration to the task of stabilization of PMLs. Our main result is formulated in Section 2, see Theorem 1. It says that given a computational domain of finite size, lacunae-based integration guarantees that the PML-generated errors will remain uniformly bounded for all times. This results holds for any linear PML, and the governing equations in the layer do not have to be modified. In Section 3, we present the results of our numerical experiments for Maxwell's equations that corroborate the theoretical design properties of the algorithm. In Section 4, we describe the decomposition of the original problem into the interior and auxiliary subproblems, which is the key element of lacunae-based ABCs [31–33]. As far as the PMLs, this decomposition will also allow us to address a much broader class of formulations than only the radiation of waves by known sources (e.g., scatterers in the domain). Finally, Section 5 contains the conclusions and some general discussion.

2. Essentials of the algorithm and the main theorem

A typical problem setup is schematically represented in Fig. 1, and it is only for the convenience of plotting that $\boldsymbol{x}$ is shown one-dimensional. In fact, we will always assume that $\boldsymbol{x} \in \mathbb{R}^3$, because lacunae exist only if the number of space dimensions is odd [26]. Accordingly, the computational domain Ω is assumed to have diameter d in $\mathbb{R}^3$. As far as its shape, from the standpoint of lacunae-based algorithms it is not important. However, the application of PMLs typically requires simple computational domains, most often Cartesian rectangles (parallelepipeds) or, sometimes, cylinders or spheres [18,22,34].

The PML surrounds the computational domain, see Fig. 1, and for simplicity we first assume that it has infinite thickness. This means that all the waves entering the PML completely die off in the layer. In practice, a PML always has finite thickness, such as in our numerical experiments of Section 3.

Let $\boldsymbol{w} = \boldsymbol{w}(\boldsymbol{x}, t)$ denote the vector of unknowns (e.g., components of the electromagnetic field or parameters of the fluid), and let it be governed by:

$$\begin{aligned} &\tfrac{\partial \boldsymbol{w}}{\partial t} + \boldsymbol{L}\boldsymbol{w} = \boldsymbol{f}(\boldsymbol{x}, t), \boldsymbol{x} \in \mathbb{R}^3, \quad t > 0, \\ &\boldsymbol{w}(\boldsymbol{x}, 0) = \boldsymbol{\varphi}, \quad \boldsymbol{x} \in \mathbb{R}^3, \end{aligned} \tag{1}$$

where the operator $\boldsymbol{L}$ is supposed to be linear and contain all the appropriate spatial derivatives of $\boldsymbol{w}$ as well as, maybe, non-differentiated terms. We require that the differential operator $\partial/\partial t + \boldsymbol{L}$ of (1) satisfies the Huygens' principle [23–28]. Mathematically, this means that the waves due to a compactly supported source (in space-time) have sharp aft fronts. In other words, at any fixed location of the observer these waves come and go, and

[3] ABCs that introduce no error due to the domain truncation.

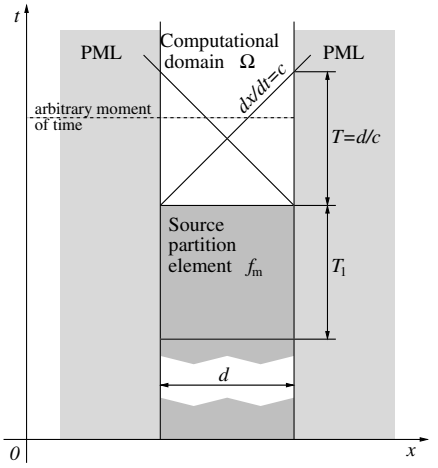

Fig. 1. Schematic.

the solution becomes identically zero after a finite interval of time. This interval is no greater than the maximum distance between the observer and the source divided by the propagation speed c (e.g., the speed of light or speed of sound).

According to [35], a scalar differential equation in the conventional $3+1$ dimensional Minkowski spacetime is Huygens' if and only if it is equivalent to the d'Alembert equation.This is a convenient criterion for practice; in particular, both Maxwell's equations [33] and linearized Euler's equations (once the entropy waves have been decoupled [32]) reduce to d'Alembert equations for individual electromagnetic or acoustic variables, and as such are Huygens'.

The right-hand side (RHS) $\boldsymbol{f}(\boldsymbol{x},t)$ in (1) represents the sources of the field; it is supposed to be compactly supported in space and may operate continuously in time: $\operatorname{supp}\boldsymbol{f} \subseteq \Omega \times [0,+\infty)$. The initial data for problem (1) are also assumed compactly supported: $\operatorname{supp}\boldsymbol{\varphi} \subseteq \Omega$. For Maxwell's equations, $\boldsymbol{f}(\boldsymbol{x},t)$ contains the extraneous electric currents, and for the acoustics equations it contains volume velocities and forces that are assumed to be given explicitly.

Let us denote by $T = d/c$ the characteristic time, which is required for the waves to cross the domain Ω, and let $T_1 > 0$, see Fig. 1. We can represent the RHS $\boldsymbol{f}(\boldsymbol{x},t)$ of (1), $\boldsymbol{x} \in \Omega$, using the partition:

$$\boldsymbol{f}(\boldsymbol{x},t) = \sum_{m=0}^{\infty} \boldsymbol{f}_m(\boldsymbol{x},t), \quad \boldsymbol{f}_m(\boldsymbol{x},t) = \begin{cases} \boldsymbol{f}(\boldsymbol{x},t), & t_m \leqslant t < t_{m+1}, \\ \boldsymbol{0}, & \text{otherwise}, \end{cases} \tag{2}$$

where $t_m = mT_1$, $m = 0,1,2,\ldots$ Next, consider the Cauchy problems:

$$\begin{aligned} &\tfrac{\partial \boldsymbol{w}_m}{\partial t} + \boldsymbol{L}\boldsymbol{w}_m = \boldsymbol{f}_m(\boldsymbol{x},t), \quad \boldsymbol{x} \in \mathbb{R}^3, \quad t > t_m, \\ &\boldsymbol{w}_m(\boldsymbol{x},t_m) = \begin{cases} \boldsymbol{\varphi}, & m = 0, \\ \boldsymbol{0}, & m > 0, \end{cases} \quad \boldsymbol{x} \in \mathbb{R}^3. \end{aligned} \tag{3}$$

Solution of problem number m from the set (3) is defined for $t \geqslant t_m \equiv mT_1$, but we can think that it is defined for all $t \geqslant 0$ and is equal to zero for $0 \leqslant t < t_m$. Then, because of the linear superposition and causality we have:

$$\boldsymbol{w}(\boldsymbol{x},t) = \sum_{m=0}^{M} \boldsymbol{w}_m(\boldsymbol{x},t), \quad \boldsymbol{x} \in \mathbb{R}^3, \quad t \geqslant 0, \tag{4}$$

where $M \stackrel{\text{def}}{=} \lceil t/T_1 \rceil - 1$, and $\lceil \alpha \rceil$ is the smallest integer $\geqslant \alpha$ (ceiling function).

Moreover, as the operator $\partial/\partial t + \boldsymbol{L}$ is Huygens', the solution of each problem (3) has a lacuna [30]. For the constant propagation speed c, the shape of the lacuna is determined by the Kirchhoff integral [26] as explained, e.g., in [29]. It is basically the common interior of all the light cones generated by a particular source. For a

given $m \geqslant 0$, the domain Ω falls into this lacuna at the moment of time $t_m + T_1 + T \equiv t_{m+1} + T$. In other words, once the source $\boldsymbol{f}_m(\boldsymbol{x}, t)$ ceases to operate (at $t = t_{m+1}$), it takes another T seconds for the waves it has generated to completely leave the domain Ω, see Fig. 1. Consequently,

$$\boldsymbol{w}_m(\boldsymbol{x}, t) = \boldsymbol{0}, \quad \boldsymbol{x} \in \Omega, \quad t \geqslant t_{m+1} + T \equiv t_{m+1} + d/c \tag{5}$$

and using (5), we can write instead of (4):

$$\boldsymbol{w}(\boldsymbol{x}, t) = \sum_{m=M_0}^{M} \boldsymbol{w}_m(\boldsymbol{x}, t), \quad \boldsymbol{x} \in \Omega, \quad t \geqslant 0, \tag{6}$$

where $M_0 \stackrel{\text{def}}{=} [(t - T)/T_1]$, and $[\cdot]$ denotes the integer part. Hence, we conclude that for any moment of time t, see Fig. 1, only so many components $\boldsymbol{w}_m$ of (3) contribute to the solution $\boldsymbol{w}(\boldsymbol{x}, t)$ of problem (1) on the domain Ω. These components are the $M - M_0 + 1$ terms in the sum (6), and their maximum number does not depend on t. Moreover, each term may only differ from zero on Ω during the interval $T_1 + T$, see (5), which does not depend on t either.

Representation of the solution $\boldsymbol{w}(\boldsymbol{x}, t)$ as *the sum of a finite non-increasing number of components* $\boldsymbol{w}_m(\boldsymbol{x}, t)$ *that each has a finite non-increasing "lifespan" on* Ω *is the key advantage provided by lacunae-based integration*; it will be of fundamental importance for our subsequent analysis. As an example, consider $T_1 = T = d/c$, see Fig. 1. Then, clearly, $M_0 = M - 1$ unless t happens to be an integer multiple of T, in which case $M_0 = M$. Consequently, the number of terms in the sum (6) in the case $T_1 = T$ is normally equal to 2 and sometimes reduces to 1. In practice, however, it will be both feasible and beneficial to take the value of T_1 several times larger than T, see Sections 3.3 and 3.4.

In reality we are not solving problem (1) directly. Instead, we are solving a combined formulation that involves the PML outside Ω (see Fig. 1):

$$\frac{\partial \boldsymbol{w}^{(\Omega)}}{\partial t} + \boldsymbol{L}\boldsymbol{w}^{(\Omega)} = \boldsymbol{f}(\boldsymbol{x}, t), \quad \boldsymbol{x} \in \Omega, \quad t > 0, \tag{7a}$$

$$\boldsymbol{w}^{(\Omega)}(\boldsymbol{x}, 0) = \boldsymbol{\varphi}, \quad \boldsymbol{x} \in \Omega,$$

$$\frac{\partial \boldsymbol{w}^{(\mathrm{PML})}}{\partial t} + \boldsymbol{L}^{(\mathrm{PML})}\boldsymbol{w}^{(\mathrm{PML})} = \boldsymbol{0}, \quad \boldsymbol{x} \in \mathbb{R}^3 \setminus \Omega, \quad t > 0,$$

$$\boldsymbol{w}^{(\mathrm{PML})}(\boldsymbol{x}, 0) = \boldsymbol{0}, \quad \boldsymbol{x} \in \mathbb{R}^3 \setminus \Omega. \tag{7b}$$

In doing so, problem (7a) is identical to (1) except that it is formulated on the bounded region Ω rather than on $\mathbb{R}^3$. For the second problem, (7b), the vector of unknowns $\boldsymbol{w}^{(\mathrm{PML})}$ typically has more components than $\boldsymbol{w}^{(\Omega)}$, and the operator $\boldsymbol{L}^{(\mathrm{PML})}$ has additional terms that render the damping of waves. It is also required that *the continuity* be enforced across the interface $\partial\Omega$:

$$\boldsymbol{w}^{(\Omega)}(\boldsymbol{x}, t) = \boldsymbol{M}\boldsymbol{w}^{(\mathrm{PML})}(\boldsymbol{x}, t), \quad \boldsymbol{x} \in \partial\Omega. \tag{7c}$$

For unsplit PMLs, the matrix $\boldsymbol{M}$ should simply match the respective components. For split PMLs, the sum of the split components in $\boldsymbol{w}^{(\mathrm{PML})}$ should be equal to the corresponding component of $\boldsymbol{w}^{(\Omega)}$. Altogether, *the ideal PML* of infinite thickness (7b), (7c) applied to the interior problem (7a) will guarantee:

$$\boldsymbol{w}^{(\Omega)}(\boldsymbol{x}, t) \equiv \boldsymbol{w}(\boldsymbol{x}, t), \quad \boldsymbol{x} \in \Omega, \quad t \geqslant 0. \tag{8}$$

The PML, however, is not ideal, and a convenient way to account for that is to introduce small perturbations $\boldsymbol{\xi}$ of the initial data. In the continuous setting these perturbations are artificial, but in reality they originate from the small residual terms of the approximation, i.e., from the truncation error [15]:

$$\frac{\partial \tilde{\boldsymbol{w}}^{(\Omega)}}{\partial t} + \boldsymbol{L}\tilde{\boldsymbol{w}}^{(\Omega)} = \boldsymbol{f}(\boldsymbol{x}, t), \quad \boldsymbol{x} \in \Omega, \quad t > 0, \tag{9a}$$

$$\tilde{\boldsymbol{w}}^{(\Omega)}(\boldsymbol{x}, 0) = \boldsymbol{\varphi} + \boldsymbol{\xi}, \quad \boldsymbol{x} \in \Omega,$$

$$\frac{\partial \tilde{\boldsymbol{w}}^{(\mathrm{PML})}}{\partial t} + \boldsymbol{L}^{(\mathrm{PML})}\tilde{\boldsymbol{w}}^{(\mathrm{PML})} = \boldsymbol{0}, \quad \boldsymbol{x} \in \mathbb{R}^3 \setminus \Omega, \quad t > 0, \tag{9b}$$

$$\tilde{\boldsymbol{w}}^{(\mathrm{PML})}(\boldsymbol{x}, 0) = \boldsymbol{\xi}, \quad \boldsymbol{x} \in \mathbb{R}^3 \setminus \Omega.$$

System (9) is to be supplemented by the same continuity condition (7c). It has been shown [6,15] that for both split and unsplit PMLs the difference between the perturbed and unperturbed solution can grow as the time elapses:

$$\|\tilde{\boldsymbol{w}}^{(\Omega)}(\cdot,t)-\boldsymbol{w}^{(\Omega)}(\cdot,t)\|\leqslant\mu(t)\|\boldsymbol{\xi}\|', \tag{10a}$$

$$\|\tilde{\boldsymbol{w}}^{(\mathrm{PML})}(\cdot,t)-\boldsymbol{w}^{(\mathrm{PML})}(\cdot,t)\|\leqslant\mu(t)\|\boldsymbol{\xi}\|'. \tag{10b}$$

The rate of growth $\mu(t)$ is determined by the particular PML; for standard PMLs it is either linear or quadratic [6,9,15]. The appropriate choice of the norms $\|\cdot\|$ and $\|\cdot\|'$ for some specific cases is discussed in [6,9,15]. Note that estimate (10b) is always sharp, because the growth of certain components of the solution inside the PML has actually been demonstrated in [9,15]. As far as the first estimate, (10a), according to [17] numerical artifacts from the PML may or may not propagate back into the domain Ω. If they don't, then $\mu(t)$ can be replaced by a true constant in (10a). We, however, will still be assuming the worst case scenario (10), for it was experimentally shown in [15,16] that the artifacts from the layer can contaminate the computational domain. Moreover, the implementation strategies that emphasize parallel efficiency may make the propagation of artifacts from the layer to the domain more likely [18].

Our goal is to show that if the plain integration of system (7) is replaced by the lacunae-based integration, then estimates (10) can be improved and made *uniform in time*. First of all, we need to see that lacunae-based integration applies to (7). In the unperturbed case, formula (8) means that if $\boldsymbol{f}(\boldsymbol{x},t)$ is partitioned according to (2), then the solutions of individual problems with the PML will still have lacunae on the domain Ω. The only difference is that the waves that leave Ω after the time T elapses will no longer travel freely but will rather be absorbed by the PML. Hence, we can write similarly to (6):

$$\boldsymbol{w}^{(\Omega)}(\boldsymbol{x},t)=\sum_{m=M_0}^{M}\boldsymbol{w}_m^{(\Omega)}(\boldsymbol{x},t),\quad \boldsymbol{x}\in\Omega,\quad t\geqslant 0, \tag{11}$$

where the individual terms $\boldsymbol{w}_m^{(\Omega)}(\boldsymbol{x},t)$, $m=0,1,2,\ldots$, satisfy [cf. (3) and (7)]:

$$\frac{\partial\boldsymbol{w}_m^{(\Omega)}}{\partial t}+\boldsymbol{L}\boldsymbol{w}_m^{(\Omega)}=\boldsymbol{f}_m(\boldsymbol{x},t),\quad \boldsymbol{x}\in\Omega,\quad t>t_m, \tag{12a}$$

$$\boldsymbol{w}_m^{(\Omega)}(\boldsymbol{x},t_m)=\begin{cases}\boldsymbol{\varphi}, & m=0\\ \boldsymbol{0}, & m>0,\end{cases}\quad \boldsymbol{x}\in\Omega,$$

$$\frac{\partial\boldsymbol{w}_m^{(\mathrm{PML})}}{\partial t}+\boldsymbol{L}^{(\mathrm{PML})}\boldsymbol{w}_m^{(\mathrm{PML})}=\boldsymbol{0},\quad \boldsymbol{x}\in\mathbb{R}^3\setminus\Omega,\quad t>t_m, \tag{12b}$$

$$\boldsymbol{w}_m^{(\mathrm{PML})}(\boldsymbol{x},t_m)=\boldsymbol{0},\quad \boldsymbol{x}\in\mathbb{R}^3\setminus\Omega,$$

$$\boldsymbol{w}_m^{(\Omega)}(\boldsymbol{x},t)=\boldsymbol{M}\boldsymbol{w}_m^{(\mathrm{PML})}(\boldsymbol{x},t),\quad \boldsymbol{x}\in\partial\Omega. \tag{12c}$$

To account for the "misbehavior" of the PML, equations (12a), (12b) need to be perturbed the same way as we have perturbed (7a), (7b) to obtain (9):

$$\frac{\partial\tilde{\boldsymbol{w}}_m^{(\Omega)}}{\partial t}+\boldsymbol{L}\tilde{\boldsymbol{w}}_m^{(\Omega)}=\boldsymbol{f}_m(\boldsymbol{x},t),\quad \boldsymbol{x}\in\Omega,\quad t>t_m, \tag{13a}$$

$$\tilde{\boldsymbol{w}}_m^{(\Omega)}(\boldsymbol{x},t_m)=\begin{cases}\boldsymbol{\varphi}+\boldsymbol{\xi}_0, & m=0\\ \boldsymbol{\xi}_m, & m>0,\end{cases}\quad \boldsymbol{x}\in\Omega,$$

$$\frac{\partial\tilde{\boldsymbol{w}}_m^{(\mathrm{PML})}}{\partial t}+\boldsymbol{L}^{(\mathrm{PML})}\tilde{\boldsymbol{w}}_m^{(\mathrm{PML})}=\boldsymbol{0},\quad \boldsymbol{x}\in\mathbb{R}^3\setminus\Omega,\quad t>t_m, \tag{13b}$$

$$\tilde{\boldsymbol{w}}_m^{(\mathrm{PML})}(\boldsymbol{x},t_m)=\boldsymbol{\xi}_m,\quad \boldsymbol{x}\in\mathbb{R}^3\setminus\Omega.$$

Solutions of the respective problems (12) and (13), (12c) will satisfy the same estimates (10) as satisfied by the solutions of (7) and (9). However, the key advantage of exploiting the lacunae is that for every $m=0,1,2,\ldots$, the corresponding system only needs to be integrated over the interval T_1+T. Hence,

$$\|\tilde{\boldsymbol{w}}_m^{(\Omega)}(\cdot,t) - \boldsymbol{w}_m^{(\Omega)}(\cdot,t)\| \leqslant C\|\boldsymbol{\xi}_m\|', \tag{14a}$$

$$\|\tilde{\boldsymbol{w}}_m^{(\mathrm{PML})}(\cdot,t) - \boldsymbol{w}_m^{(\mathrm{PML})}(\cdot,t)\| \leqslant C\|\boldsymbol{\xi}_m\|', \tag{14b}$$

where $C = \mu(T_1 + T)$ is a constant. Another key advantage of using lacunae is a finite and non-increasing number of summation terms in formula (11). Combined with estimate (14a), formula (11) yields (by the triangle inequality):

$$\|\tilde{\boldsymbol{w}}^{(\Omega)}(\cdot,t) - \boldsymbol{w}^{(\Omega)}(\cdot,t)\| \leqslant C_0 \sup_m \|\boldsymbol{\xi}_m\|', \tag{15a}$$

where $C_0 = C \cdot (M - M_0 + 1)$ and the norms $\|\boldsymbol{\xi}_m\|'$ are assumed bounded altogether. In contradistinction to (10a), estimate (15a) implies that even if the PML errors contaminate Ω, *the resulting error on Ω will remain uniformly bounded for all times*. Note that according to (8), $\boldsymbol{w}^{(\Omega)}(\cdot,t)$ can be replaced with $\boldsymbol{w}(\cdot,t)$ on the left-hand side of (15a), which means that we have proved:

Theorem 1. *Let $\Omega \subset \mathbb{R}^3$ be a bounded domain, and let problem (1) be solved using a PML around Ω combined with the lacunae-based algorithm, see (11) and (12). Then, assuming that* $\sup_m \|\boldsymbol{\xi}_m\|' < \infty$, *the error on Ω due to the perturbation* (13) *of the PML will remain uniformly bounded for all times*:

$$\|\tilde{\boldsymbol{w}}^{(\Omega)}(\cdot,t) - \boldsymbol{w}(\cdot,t)\|_\Omega \leqslant C_0 \sup_m \|\boldsymbol{\xi}_m\|'. \tag{15b}$$

Estimate (15b) provides an error bound for the domain Ω. In fact, the error growth inside the PML is also uniformly bounded, i.e., an estimate similar to (15b) holds for the complementary domain $\mathbb{R}^3 \setminus \Omega$ as well. It, however, should be written differently:

$$\left\| \sum_{m=M_0}^{M} \tilde{\boldsymbol{w}}_m^{(\mathrm{PML})}(\cdot,t) - \sum_{m=M_0}^{M} \boldsymbol{w}_m^{(\mathrm{PML})}(\cdot,t) \right\| \leqslant C_0 \sup_m \|\boldsymbol{\xi}_m\|'. \tag{15c}$$

The first and second terms on the left-hand side of (15c) are solutions in the PML with and without perturbations, respectively. They are left in the form of the sums because the lossy equations of the PML shall not be expected to be Huygens', and formula (11) will not, generally speaking, hold. In other words, since the solution is represented as a finite sum of terms with finite lifespan, the uniform bound (15c) is guaranteed. However, unlike on Ω, the solutions obtained in the PML with and without lacunae will not be the same.

3. Numerical experiments

In this section, we demonstrate the performance of the algorithm introduced in Section 2.

3.1. Computational setup

For the purpose of relating to prior work, in our numerical experiments we would like to stay as close as possible to the setup of [15]; a very similar setup was also used in our recent paper [16]. The two key differences between the simulations in the current paper and those conducted in [15,16] are that here we are using cylindrically symmetric geometry so that to be able to take advantage of the three-dimensional effects (lacunae) in an essentially two-dimensional setting, and also that in [15,16] the solution was driven by the initial conditions whereas here it is driven by a continuously operating source term on the right-hand side (described in Section 3.2).

3.1.1. Governing equations and geometry

Let r, z, and θ denote the cylindrical coordinates; the assumption of axial (cylindrical) symmetry implies that all the derivatives with respect to the polar angle vanish: $\frac{\partial}{\partial\theta} \equiv 0$. Then, the full Maxwell system of equations gets split into two independent subsystems that correspond to the transverse magnetic (TM) and transverse electric (TE) modes. Following [15,16], we will be solving the TE Maxwell equations in vacuum (c is the speed of light):

$$\begin{aligned}
&\frac{1}{c}\frac{\partial E_r}{\partial t}+\frac{\partial H_\theta}{\partial z}=-\frac{4\pi}{c}j_r,\\
&\frac{1}{c}\frac{\partial E_z}{\partial t}-\frac{1}{r}\frac{\partial (rH_\theta)}{\partial r}=-\frac{4\pi}{c}j_z,\\
&\frac{1}{c}\frac{\partial H_\theta}{\partial t}-\left(\frac{\partial E_z}{\partial r}-\frac{\partial E_r}{\partial z}\right)=0,
\end{aligned} \tag{16}$$

where E_r and E_z denote the radial and axial components of the electric field, respectively, and H_θ denotes the angular component of the magnetic field. The first two equations in system (16) represent the Ampère law and are driven by the extraneous electric current with the components j_r and j_z. The third equation in (16) represents the Faraday law and is homogeneous (no magnetic currents). The unsteady equations (16) are supplemented by the steady-state equation

$$\frac{1}{r}\frac{\partial (rE_r)}{\partial r}+\frac{\partial E_z}{\partial z}=4\pi\rho, \tag{17}$$

where ρ is the electric charge density. Eq. (17) is the Gauss law of electricity, it relates the flux of the electric field through a given closed surface to the charge contained inside. A necessary solvability condition for system (16) and (17) is the continuity equation that represents the conservation of charge:

$$\frac{\partial \rho}{\partial t}+\frac{1}{r}\frac{\partial (rj_r)}{\partial r}+\frac{\partial j_z}{\partial z}=0. \tag{18}$$

As long as condition (18) holds for the source terms ρ, j_r, and j_z, the steady-state Eq. (17) can be left out of the consideration when time-marching the unsteady Eq. (16).

At the axis of the cylindrical system, Maxwell's equations require additional attention. Under the natural assumption that all the physical quantities involved must be continuous and bounded, one can easily see that the vector components H_θ, E_r, and j_r can only meet the constraint of axial symmetry if they vanish at $r=0$:

$$H_\theta(t,r,z)|_{r=0}=0,\quad E_r(t,r,z)|_{r=0}=0,\quad j_r(t,r,z)|_{r=0}=0. \tag{19}$$

The axial components E_z and j_z do not have to vanish, although given (19), the third equation of system (16) reduces to $\frac{\partial E_z}{\partial r}|_{r=0}=0$. The first equation of system (16) reduces to the identity $0=0$ on the axis, and the only equation that does not degenerate is the second equation. Taking into account the first equality from (19), we can use the Taylor formula for $r\ll 1$ and write: $H_\theta(t,r,z)=\frac{\partial H_\theta}{\partial r}|_{r=0}\cdot r+\mathcal{O}(r^2)$. Consequently, $\frac{1}{r}\frac{\partial (rH_\theta)}{\partial r}=\frac{1}{r}\frac{\partial H_\theta}{\partial r}|_{r=0}\cdot\frac{\partial r^2}{\partial r}+\mathcal{O}(r)$, which yields: $\frac{1}{r}\frac{\partial (rH_\theta)}{\partial r}|_{r=0}=2\frac{\partial H_\theta}{\partial r}|_{r=0}$. Therefore, on the axis we have:

$$\frac{1}{c}\frac{\partial E_z}{\partial t}-2\frac{\partial H_\theta}{\partial r}=-\frac{4\pi}{c}j_z. \tag{20}$$

The geometry of the problem is schematically shown in Fig. 2. The computational domain has a rectangular shape in the (r,z) variables:

$$\Omega=\{(r,z)\|0\leqslant r\leqslant 5,-5\leqslant z\leqslant 5\}.$$

The currents (and charges) that drive the solution, see equations (16), (17), are assumed to be compactly supported in space on the ball $R\equiv(r^2+z^2)^{1/2}\leqslant R_0$, and we typically choose $R_0=3$. The computational domain is terminated by the PML of width $l=1$ in the axial direction, see Fig. 2. In fact, with the proper choice of damping the width of the layer beyond a certain point no longer affects the quality of the solution on Ω (see Section 3.4).

3.1.2. PML

For our computations we take the mathematically derived unsplit PML of [13]. In the experiments of [16], this layer has clearly shown to be prone to the undesirable growth of the solution for long integration times. We note that originally the PML of [13] was constructed for the two-dimensional Cartesian TE Maxwell equations. As, however, the axial coordinate of the cylindrical system is essentially Cartesian, the layer of [13] can be exported to the setup shown in Fig. 2 with no change at all:

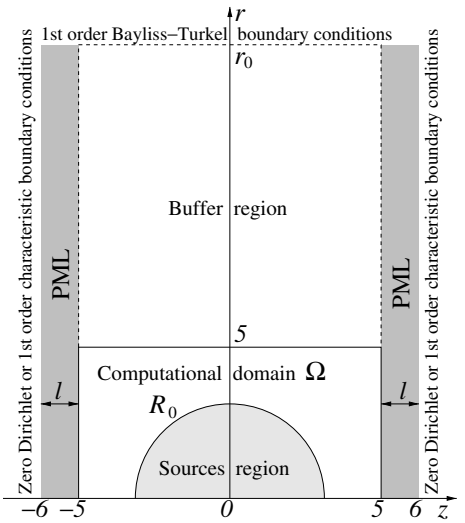

Fig. 2. Geometric setup in the space.

$$
\begin{aligned}
&\frac{1}{c}\frac{\partial E_r}{\partial t}+\frac{\partial H_\theta}{\partial z}=-2\sigma E_r-\sigma P,\\
&\frac{1}{c}\frac{\partial E_z}{\partial t}-\frac{1}{r}\frac{\partial (rH_\theta)}{\partial r}=0,\\
&\frac{1}{c}\frac{\partial H_\theta}{\partial t}-\left(\frac{\partial E_z}{\partial r}-\frac{\partial E_r}{\partial z}\right)=\sigma' Q,\\
&\frac{1}{c}\frac{\partial P}{\partial t}=\sigma E_r,\\
&\frac{1}{c}\frac{\partial Q}{\partial t}=-\sigma Q-E_r.
\end{aligned}
\tag{21}
$$

Note that the PML (21) is built for the homogeneous Maxwell equations, because the right-hand sides of system (16), i.e., the currents, may only differ from zero for $R \leqslant R_0$ and hence vanish near the outer boundary of Ω, see Fig. 2. Compared to (16), system (21) contains two additional unknown quantities, $P = P(t,r,z)$ and $Q = Q(t,r,z)$. These quantities are identically equal to zero on Ω, and in the layer they are governed by two additional ordinary differential equations. The quantity $\sigma = \sigma(z)$ in (21) is the damping coefficient. It is also identically zero on Ω, whereas in the PML a certain degree of flexibility exists in choosing σ. In our computations, we will follow the recommendation of [15] and define:

$$
\sigma(z)=\begin{cases}\sigma_0\left(\frac{5-z}{l}\right)^3, & -5-l\leqslant z\leqslant -5,\\ 0, & -5<z<5,\\ \sigma_0\left(\frac{z-5}{l}\right)^3, & 5\leqslant z\leqslant 5+l.\end{cases}
\tag{22}
$$

For the PML of width $l = 1$, see Fig. 2, we normally take $\sigma_0 = 10$ in (22).

3.1.3. Boundary conditions

The PML itself is terminated at $z = 5 + l$ and $z = -5 - l$ either by zero Dirichlet boundary conditions for all field variables or by locally one-dimensional characteristic boundary conditions. Again, as indicated in Section 3.4, if the damping inside the layer is sufficiently strong, the boundary conditions at the outer boundaries of the PML make little or no difference as far as the quality of the solution on Ω. The use of characteristic boundary conditions, however, may bring along an additional benefit. With these boundary conditions, if the layer is switched off (i.e., if $\sigma \equiv 0$ everywhere), the boundary still has some non-reflecting properties suf-

ficient for computing the solution with a "non-catastrophic" accuracy over a reasonably long time interval. This computation (see Section 3.4) allows us to unambiguously attribute the undesirable long-term growth to the presence of the PML, because having the PML switched on or off appears the only difference between the two otherwise identical settings. Note that a similar argument was previously used in [16] for identifying the roots of the long-time growth of the solution.

The quasi-one-dimensional characteristic boundary conditions are set at the outer boundaries of the PML by artificially disregarding the r derivatives in system (16) and setting to zero the incoming Riemann variables. In doing so, we are disregarding the PML (21) near the boundary and setting the boundary conditions for the homogeneous version of Maxwell's equations (16). In the quasi-one-dimensional z framework, we consider two equations:

$$\frac{1}{c}\frac{\partial E_r}{\partial t}+\frac{\partial H_\theta}{\partial z}=0 \quad \text{and} \quad \frac{1}{c}\frac{\partial H_\theta}{\partial t}+\frac{\partial E_r}{\partial z}=0. \tag{23}$$

By adding and subtracting Eq. (23) to/from one another, we realize that the Riemann variable $H_\theta - E_r$ is incoming at $z = 5 + l$ and the Riemann variable $H_\theta + E_r$ is incoming at $z = -5 - l$, see Fig. 2. Consequently, the desired characteristic boundary conditions are:

$$H_\theta - E_r|_{r=5+l} = 0 \quad \text{and} \quad H_\theta + E_r|_{r=-5-l} = 0. \tag{24}$$

The far field treatment that we adopt for the radial direction differs from the one in the axial direction. An unsplit PML similar to (21) but built for the genuinely cylindrical setting[4] is not readily available. Therefore, we have decided to introduce a large buffer region and terminate it with the first order Bayliss–Turkel local boundary conditions [36–39]. For the size of the domain Ω in the radial direction equal to 5, we may take, e.g., $r_0 = 15$, see Fig. 2. The motivation is that as the amplitude of the waves generated by the sources inside Ω decays proportionally to $R^{-1} \equiv (r^2 + z^2)^{-1/2}$, for a sufficiently remote boundary $r = r_0$ the magnitude of the reflections produced by the Bayliss–Turkel boundary conditions will be small. The computations of Section 3.4 corroborate that the magnitude of those reflections can indeed be driven down below the truncation error level inside Ω.

The Bayliss–Turkel boundary conditions are standard, but their derivation for system (16) requires a little extra care. As for any quasi-one-dimensional treatment, we disregard tangential derivatives (i.e., z derivatives) at the boundary $r = r_0$ and from the homogeneous Maxwell equations obtain the following independent second order equations for the filed components E_z and H_θ:

$$\frac{1}{c^2}\frac{\partial^2 E_z}{\partial t^2}=\frac{1}{r}\frac{\partial}{\partial r}\left(r\frac{\partial E_z}{\partial r}\right), \tag{25a}$$

$$\frac{1}{c^2}\frac{\partial^2 H_\theta}{\partial t^2}=\frac{\partial}{\partial r}\left(\frac{1}{r}\frac{\partial (rH_\theta)}{\partial r}\right). \tag{25b}$$

Eq. (25a) is the standard scalar d'Alembert equation, because E_z is a Cartesian vector component. Eq. (25b) is a vector d'Alembert equation, because H_θ is a non-Cartesian component. In the frequency space, Eqs. (25a) and (25b) transform into

$$\frac{\partial^2 \widehat{E}_z}{\partial r^2}+\frac{1}{r}\frac{\partial \widehat{E}_z}{\partial r}+\frac{\omega^2}{c^2}\widehat{E}_z=0, \tag{26a}$$

$$\frac{\partial^2 \widehat{H}_\theta}{\partial r^2}+\frac{1}{r}\frac{\partial \widehat{H}_\theta}{\partial r}-\frac{1}{r^2}\widehat{H}_\theta+\frac{\omega^2}{c^2}\widehat{H}_\theta=0. \tag{26b}$$

Eq. (26a) is a Bessel equation of order $\nu = 0$ and Eq. (26b) is a Bessel equation of order $\nu = 1$ because they can both be reduced to the respective standard forms by the change of variable $y = kr$, where $k = \omega/c$. Accordingly, the radiation solutions of these equations are given by the Hankel functions $H_\nu^{(2)}(kr)$, where $\nu = 0$ corresponds to (26a) and $\nu = 1$ corresponds to (26b). Therefore, the radiation boundary conditions can be

[4] Recall, unlike z, r of the cylindrical system is not a Cartesian variable.

obtained by requiring that the desired solution be parallel to $H_\nu^{(2)}(kr)$ in the sense of the corresponding Wronskian (see [2, Section 1.2]):

$$\frac{\partial \widehat{E}_z}{\partial r} - \widehat{E}_z \frac{\frac{\partial}{\partial r} H_0^{(2)}(kr)}{H_0^{(2)}(kr)} = 0, \tag{27a}$$

$$\frac{\partial \widehat{H}_\theta}{\partial r} - \widehat{H}_\theta \frac{\frac{\partial}{\partial r} H_1^{(2)}(kr)}{H_1^{(2)}(kr)} = 0. \tag{27b}$$

For large arguments y, the Hankel functions have the following asymptotic:

$$H_\nu^{(2)}(y) = \sqrt{\frac{2}{\pi y}} \mathrm{e}^{-\mathrm{i}(y - \frac{\pi\nu}{2} - \frac{\pi}{4})} + \mathcal{O}(y^{-\frac{3}{2}})$$

so that for any ν we have:

$$\frac{\mathrm{d}}{\mathrm{d}y} H_\nu^{(2)}(y) \approx -\frac{1}{2y} H_\nu^{(2)}(y) - iH_\nu^{(2)}(y),$$

and consequently,

$$\frac{\mathrm{d}}{\mathrm{d}r} H_\nu^{(2)}(kr) \approx \left(-\frac{1}{2r} - ik\right) H_\nu^{(2)}(kr).$$

Therefore, disregarding the residual terms of the asymptotic, we can write instead of (27a), (27b):

$$\frac{\partial \widehat{E}_z}{\partial r} + \frac{1}{2r}\widehat{E}_z + \mathrm{i}k\widehat{E}_z = 0, \tag{28a}$$

$$\frac{\partial \widehat{H}_\theta}{\partial r} + \frac{1}{2r}\widehat{H}_\theta + \mathrm{i}k\widehat{H}_\theta = 0. \tag{28b}$$

Back in the time domain, boundary conditions (28a), (28b) transform into

$$\frac{1}{c}\frac{\partial E_z}{\partial t} + \frac{\partial E_z}{\partial r} + \frac{1}{2r}E_z = 0, \tag{29a}$$

$$\frac{1}{c}\frac{\partial H_\theta}{\partial t} + \frac{\partial H_\theta}{\partial r} + \frac{1}{2r}H_\theta = 0 \tag{29b}$$

and we realize that in the end of the day both field variables, E_z and H_θ, satisfy the same boundary condition even though the governing Eqs. (25a) and (25b) are different. The Bayliss–Turkel boundary conditions (29a) and (29b) are to be set at the far field boundary $r = r_0$, see Fig. 2.

3.1.4. Discretization

The problem we have described is discretized on the grid with square cells: $h_z = h_r = h$. To demonstrate the convergence, we actually use a sequence of grids in Section 3.4 with $h = 0.1, 0.05, 0.025$, and 0.0125. The spatial derivatives in system (16) (as well as in (17)) are approximated by central differences with second order accuracy, and the temporal derivatives are approximated by the conventional fourth order Runge–Kutta method (see, e.g., [40, Section 9.4]). The overall scheme is standard and we therefore do not write it out explicitly except for the approximation of the radial derivative:

$$\frac{1}{r}\frac{\partial(rH_\theta)}{\partial r}\Big|_n = \frac{1}{r_n}\frac{r_{n+1}H_{\theta n+1} - r_{n-1}H_{\theta n-1}}{2h} + \mathcal{O}(h^2),$$

where $r_n = nh$, $n = 0, 1, 2, \ldots$ The same scheme was used in [16] in the Cartesian case, and it led to the growth of the solution inside the PML.

The spatial derivatives in the on-axis Eq. (17) and in the boundary conditions (29a) and (29b) are approximated by one-sided differences with second order accuracy, and all temporal derivatives, including those of P and Q in the PML (21) are approximated by the same Runge–Kutta scheme.

The characteristic boundary conditions (24) are approximated in the context of Runge–Kutta time marching. Let τ be the time step and assume that the right boundary $z = 5 + l = 6$, see Fig. 2, corresponds to $m = M$ on the grid. At the first stage of Runge–Kutta, we write for the first Eq. (23):

$$\widetilde{E}_{rM} = E_{rM} - \frac{c\tau}{2}\frac{H_{\theta M+1} - H_{\theta M-1}}{2h}$$

and combine it with the second order approximation of the first Eq. (24):

$$E_{rM} = \frac{H_{\theta M+1} + H_{\theta M-1}}{2}.$$

Then, eliminating the ghost variable $H_{\theta M+1}$, we obtain:

$$\widetilde{E}_{rM} = E_{rM}\left(1 - \frac{c\tau}{2h}\right) + \frac{c\tau}{2h}H_{\theta M-1} \tag{30a}$$

and likewise for the magnetic field with the help of the second Eq. (23):

$$\widetilde{H}_{\theta M} = H_{\theta M}\left(1 - \frac{c\tau}{2h}\right) + \frac{c\tau}{2h}E_{rM-1}. \tag{30b}$$

Relations (30a) and (30b) are the discrete characteristic boundary conditions. Similar relations can be obtained for other stages of Runge–Kutta and for the opposite boundary $z = -5 - l \Longleftrightarrow m = -M$.

3.2. Test solution

To study the performance of the algorithm, we would like to be able to compute the actual numerical error on the grid at different moments of time. As such, we need the exact solution, and we obtain it by "backward engineering."

We begin with the standard scalar retarded potential:

$$\phi = \frac{\chi(t - R/c)}{R} \tag{31}$$

that solves the three-dimensional d'Alembert equation driven by the source term $4\Pi\,\delta(\boldsymbol{x}) \cdot \chi(t)$, where $R = |\boldsymbol{x}|$. The modulating function $\chi(t)$ is assumed to be sufficiently smooth for $-\infty < t < \infty$ and $\chi(t) \equiv 0$ for $t < 0$.Along with the cylindrical coordinates (r, θ, z), let us also consider the Cartesian coordinates (x, y, z), so that $x = r\cos\theta$, $y = r\sin\theta$, and $R^2 = r^2 + z^2 = x^2 + y^2 + z^2$. By differentiating the retarded potential ϕ of (31), we obtain:

$$\phi'_x = \left[-\frac{\chi(t - R/c)}{R^2} - \frac{1}{c}\frac{\chi'(t - R/c)}{R}\right]\frac{x}{R}, \tag{32a}$$

$$\phi'_y = \left[-\frac{\chi(t - R/c)}{R^2} - \frac{1}{c}\frac{\chi'(t - R/c)}{R}\right]\frac{y}{R}. \tag{32b}$$

The derivatives $\phi'_x \equiv \frac{\partial\phi}{\partial x}$ and $\phi'_y \equiv \frac{\partial\phi}{\partial y}$ are solutions of the d'Alembert equation driven by the dipoles $4\Pi\,\delta'_x(\boldsymbol{x}) \cdot \chi(t)$ and $4\Pi\,\delta'_y(\boldsymbol{x}) \cdot \chi(t)$, respectively.

Next, we introduce a new vector field $\boldsymbol{B}$ by defining its Cartesian components:

$$B_x = -\phi'_y, \quad B_y = \phi'_x, \quad B_z = 0,$$

where ϕ'_x and ϕ'_y are given by (32a) and (32b), respectively. For the cylindrical components of $\boldsymbol{B}$ we therefore have:

$$B_\theta = -\sin\theta B_x + \cos\theta B_y = \left[-\frac{\chi(t - R/c)}{R^2} - \frac{1}{c}\frac{\chi'(t - R/c)}{R}\right]\frac{r}{R}, \tag{33a}$$

$$B_r = \cos\theta B_x + \sin\theta B_y = 0. \tag{33b}$$

By design, the vector field $\boldsymbol{B} = \boldsymbol{B}(\boldsymbol{x}, t)$ is a solution to the three-dimensional vector d'Alembert equation driven by the following dipole at the origin:

$$4\Pi(-\delta_y'(\boldsymbol{x}), \delta_x'(\boldsymbol{x}), 0)\cdot\chi(t).$$

This solution is axially symmetric, because $\frac{\partial B_\theta}{\partial\theta}=0$. This solution is also singular at the origin. Therefore, we introduce a scalar multiplier function $\psi=\psi(R)$ that should have at least p continuous derivatives for $R\geqslant 0$. We require that $\psi(R)\equiv 1$ for $R\geqslant R_0$, see Fig. 2, and $\psi(0)=\psi\prime(0)=\cdots=\psi^{(p)}(0)=0$. In practice, we take $p=6$ and build $\psi(R)$ on $0\leqslant R\leqslant R_0$ as a polynomial of degree 13.

Having constructed $\psi(R)$, we introduce a new vector field $\widetilde{\boldsymbol{B}}(\boldsymbol{x},t)=\boldsymbol{B}(\boldsymbol{x},t)\cdot\psi(R)$, which no longer has a singularity at the origin. Moreover, it even turns into zero at $R=0$ along with at least $p-2$ of its derivatives, see formula (33a). Note that for $R>R_0$ the vector field $\widetilde{\boldsymbol{B}}(\boldsymbol{x},t)$ is still an axially symmetric solution to the homogeneous three-dimensional d'Alembert equation. The test solution for Maxwell's equations (16) will be obtained by using $\widetilde{\boldsymbol{B}}(\boldsymbol{x},t)$ as a generating function for the vector potential of the electromagnetic field.

It is well known that even though the three-dimensional electromagnetic field consists of two vector quantities, the electric field $\boldsymbol{E}$ and the magnetic field $\boldsymbol{H}$ (six scalar components altogether), there are, in fact, only four independent scalar quantities that determine the field. These four quantities are conveniently represented as the vector potential $\boldsymbol{A}$ and the scalar potential φ. Moreover, the vector and scalar potentials are not defined uniquely either, they may be required to satisfy additional constraints. Each particular form of $\boldsymbol{A}$ and φ under a given set of constraints is known as a gauge, and the independence of $\boldsymbol{E}$ and $\boldsymbol{H}$ on the specific choice of the gauge is known as gauge invariance [41, Chapter 3]. The Coulomb gauge corresponds to $\varphi\equiv 0$, then

$$\boldsymbol{E}=-\frac{1}{c}\frac{\partial\boldsymbol{A}}{\partial t}\quad\text{and}\quad\boldsymbol{H}=\operatorname{curl}\boldsymbol{A}. \tag{34}$$

Let us define the vector potential as $\boldsymbol{A}=\operatorname{curl}\widetilde{\boldsymbol{B}}$ so that

$$A_r=-\frac{\partial\widetilde{B}_\theta}{\partial z},\quad A_z=\frac{1}{r}\frac{\partial(r\widetilde{B}_\theta)}{\partial r},\quad\text{and}\quad A_\theta=0. \tag{35}$$

The vector potential $\boldsymbol{A}=\boldsymbol{A}(t,r,z)$ is also a solution to the three-dimensional d'Alambert equation; this equation is homogeneous for $R>R_0$ and inhomogeneous for $R\leqslant R_0$. The specific form of inhomogeneity for $\boldsymbol{A}$ can be derived, but it is of no immediate importance, because what we need is the right-hand sides of the Maxwell equations that drive the fields.

Using the definition of vector potential (35) and applying transformation (34), we obtain the following components of electromagnetic field:

$$\begin{aligned}E_z(t,r,z)=&-\frac{1}{c^3R^6}(c^2\chi'(t-R/c)((r^2-2z^2)R\psi(R)-r^2R^2\psi'(R))+R^2(-cr^2R\psi'(R)\chi''(t-R/c)\\&+\psi(R)(c(r^2-2z^2)\chi''(t-R/c)+r^2R\chi^{(3)}(t-R/c)))),\end{aligned} \tag{36a}$$

$$\begin{aligned}E_r(t,r,z)=&-\frac{rz}{c^3R^6}(c^2\chi'(t-R/c)(-3R\psi(R)+R^2\psi'(R))-R^2(-cR\psi'(R)\chi''(t-R/c)\\&+\psi(R)(3c\chi''(t-R/c)+R\chi^{(3)}(t-R/c))))\end{aligned} \tag{36b}$$

and

$$\begin{aligned}H_\theta(t,r,z)=&\frac{r}{c^3R^5}(c^3\chi(t-R/c)(-2R\psi'(R)+R^2\psi''(R))-R^2(2cR\psi'(R)\chi''(t-R/c)\\&+c^2\chi'(t-R/c)(2\psi'(R)-R\psi''(R))-\psi(R)(c\chi''(t-R/c)+R\chi^{(3)}(t-R/c)))).\end{aligned} \tag{36c}$$

By design, the fields given by (36a), (36b), (36c) solve the Maxwell equations (16), and the resulting currents j_r and j_z that we calculate below are non-zero only for $R\leqslant R_0$. Moreover, as according to (34) $\operatorname{div}\boldsymbol{E}=-\frac{1}{c}\frac{\partial\operatorname{div}\boldsymbol{A}}{\partial t}$, and $\boldsymbol{A}=\operatorname{curl}\widetilde{\boldsymbol{B}}$, the electric field of (36a), (36b) is solenoidal, $\operatorname{div}\boldsymbol{E}=0$, and consequently, the continuity Eq. (18) is satisfied identically.

The currents j_r and j_z are obtained by substituting the fields (36a), (36b), (36c) into the first two equations of system (16):

$$-\frac{4\pi}{c}j_z(t,r,z) = \frac{1}{c^3R^7}(-c^3\chi(t-R/c)(4(r^2-z^2)R\psi'(R) - R^2((3r^2-2z^2)\psi''(R) - r^2R\psi^{(3)}(R)))$$
$$- R^2(-3cr^2R^2\chi''(t-R/c)\psi''(R) + 2\psi'(R)(c(r^2-2z^2)R\chi''(t-R/c) + r^2R^2\chi^{(3)}(t-R/c))$$
$$+ c^2\chi'(t-R/c)(4(r^2-z^2)\psi'(R) + R(-3r^2+2z^2)\psi''(R) + r^2R^2\psi^{(3)}(R)))), \tag{37a}$$

$$-\frac{4\pi}{c}j_r(t,r,z) = \frac{rz}{c^3R^7}(c^3\chi(t-R/c)(8R\psi'(R) - R^2(5\psi''(R) - R\psi^{(3)}(R))) + R^2(-3cR^2\chi''(t-R/c)\psi''(R)$$
$$+ 2\psi'(R)(3cR\chi''(t-R/c) + R^2\chi^{(3)}(t-R/c))$$
$$+ c^2\chi'(t-R/c)(8\psi'(R) - 5R\psi''(R) + R^2\psi^{(3)}(R)))). \tag{37b}$$

By design, the solution of Maxwell's equations (16) driven by the currents (37a) and (37b) and subject to the homogeneous initial conditions is given by the fields (36a)–(36c). In Section 3.4, we solve system (16) with the right-hand sides (37a) and (37b) numerically and evaluate the error by comparing the solution computed on the grid with the exact solution (36a)–(36c).

3.3. Implementation issues

An important consideration to be addressed when implementing the strategy of Section 2 in a computational setting is how to preserve the lacunae in the numerical solution. It is clear that a straightforward partition of the continuously operating source according to formula (2) may create discontinuities at the splitting points t_m, $m = 0, 1, 2, \ldots$, even if the function $\boldsymbol{f}(\boldsymbol{x}, t)$ itself is smooth. From the standpoint of the original Huygens' principle, having a discontinuous right-hand side presents no problem, and the sharp aft fronts will remain sharp aft fronts. In the discrete context, however, the discontinuities may lead to the deterioration (or loss) of consistency by the scheme, and the aft fronts will then be "smeared out" by numerical artifacts.

Therefore, following our previous work [29,31–33], we introduce an alternative approach to partitioning the RHS $\boldsymbol{f}(\boldsymbol{x}, t)$. Consider a smooth partition of unity schematically shown in Fig. 3. Let T_0 be the size (duration) of each partition element, and ΔT be the width (duration) of the transition zone. Denote by $\zeta(t)$ the smooth compactly supported function that renders the partition so that $\zeta(t) \equiv 1$ for $\Delta T \leqslant t \leqslant T_0 - \Delta T$ and $\zeta(t) + \zeta(t - (T_0 - \Delta T)) \equiv 1$ for $T_0 - \Delta T < t < T_0$. Then, the individual partition elements are obtained by a mere translation: $\zeta(t - m(T_0 - \Delta T))$, $m = -1, 0, 1, 2, \ldots$

Having introduced the partition of unity shown in Fig. 3, we redefine the partition of the RHS (2) as follows. Let $T_1 \stackrel{\text{def}}{=} T_0 - \Delta T$, then

$$\boldsymbol{f}(\boldsymbol{x}, t) = \sum_{m=0}^{\infty} \boldsymbol{f}_m(\boldsymbol{x}, t),$$
$$\boldsymbol{f}_m(\boldsymbol{x}, t) = \begin{cases} \boldsymbol{f}(\boldsymbol{x}, t) \cdot \zeta(t - mT_1), & t_m \leqslant t < t_{m+1} + \Delta T, \\ \boldsymbol{0}, & \text{otherwise}, \end{cases} \tag{38}$$

where $t_m = mT_1$, $m = 0, 1, 2, \ldots$ Formula (38) applies uniformly to all $m = 0, 1, 2, \ldots$ except that no change of the RHS is needed near $t = 0$ and $\boldsymbol{f}_0(\boldsymbol{x}, t) \equiv \boldsymbol{f}(\boldsymbol{x}, t)$ for $0 \leqslant T \leqslant \Delta T$. The key difference between the new partition (38) and the previous partition (2) is that as long as $\boldsymbol{f}(\boldsymbol{x}, t)$ is smooth, all $\boldsymbol{f}_m(\boldsymbol{x}, t)$ defined by formula (38) are also smooth. Hence, no loss of consistency shall be expected for any discretization applied to individual subproblems (3) or (12). Therefore, the corresponding numerical solutions will have the lacunae approximated on the grid with the accuracy that pertains to the specific scheme.

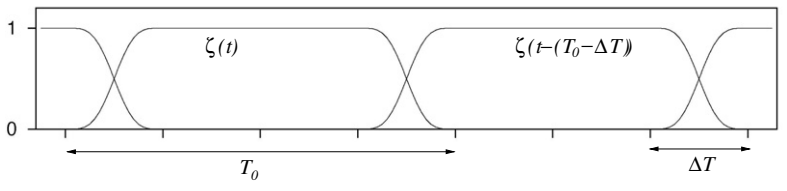

Fig. 3. Smooth partition of unity.

The use of the overlapping partition (38) instead of (2) causes only minor changes in the algorithm of Section 2. In fact, all the formulae stay the same, and only instead of (5) we now write:

$$\boldsymbol{w}_m(\boldsymbol{x},t)=\boldsymbol{0},\quad \boldsymbol{x}\in\Omega,\quad t\geqslant t_{m+1}+\Delta T+T\equiv t_{m+1}+\Delta T+d/c, \tag{39}$$

because the source $\boldsymbol{f}_m(\boldsymbol{x},t)$ ceases to operate at $t=t_{m+1}+\Delta T$ rather than at $t=t_{m+1}$, as in Section 2. Accordingly, in formula (6) we need to redefine the lower summation index: $M_0\overset{\text{def}}{=}[(t-\Delta T-T)/T_1]$, where $[\cdot]$ denotes the integer part, as before. In the computations of Section 3.4, the value of T_0 is typically taken much larger than ΔT, see Fig. 3, and even a few times larger than $T=d/c$. This, in particular, means that we always have $t_m+\Delta T+T<t_{m+1}$. Consequently, the number of terms $M-M_0+1$ in the sum (6) is equal to either 2 or 1. Namely,

$$M-M_0+1=\begin{cases}2, & \text{if } t_m\leqslant t\leqslant t_m+\Delta T+T,\\ 1, & \text{if } t_m+\Delta T+T<t<t_{m+1}.\end{cases} \tag{40}$$

It should also be noted that in the context of Maxwell's equations (16), the RHS $\boldsymbol{f}(\boldsymbol{x},t)$ is given by the components of the current j_r and j_z. In the test solution of Section 3.2, the current (37a) and (37b) is constructed solenoidal, and the charge density ρ is zero, so that the continuity Eq. (18) is satisfied identically. Obviously, the partition (38) will keep the current solenoidal, and hence the necessary solvability condition (18) for Maxwell's equations will automatically hold for every individual subproblem (3).

3.4. Results of computations

The modulating function $\chi(t)$ that we take for our experiments is

$$\chi(t)=\begin{cases}\sum\limits_{j=1}^{j=4}a_j\sin(\omega_j t), & \text{if } t\geqslant 0,\\ 0, & \text{if } t<0,\end{cases} \tag{41}$$

where the frequencies ω_j, $j=1,\ldots,4$, are chosen incommensurate:

$$\omega_1=1,\quad \omega_2=\sqrt{3/2}\omega_1,\quad \omega_3=\sqrt{2}\omega_1,\quad \omega_4=\sqrt{3}\omega_1$$

so that to avoid periodicity, and the coefficients a_j, $j=1,\ldots,4$, are given by

$$a_1=-\frac{1}{\omega_1(\omega_1^2-\omega_2^2)(\omega_1^2-\omega_3^2)(\omega_1^2-\omega_4^2)},$$

$$a_2=-\frac{1}{\omega_2(\omega_2^2-\omega_1^2)(\omega_2^2-\omega_3^2)(\omega_2^2-\omega_4^2)},$$

$$a_3=-\frac{1}{\omega_3(\omega_3^2-\omega_1^2)(\omega_3^2-\omega_2^2)(\omega_3^2-\omega_4^2)},$$

$$a_4=-\frac{1}{\omega_4(\omega_4^2-\omega_1^2)(\omega_4^2-\omega_2^2)(\omega_4^2-\omega_3^2)},$$

which guarantees that $\chi(t)$ of (41) and its derivatives up to order 6 are continuous on the entire line $(-\infty,\infty)$, while $\chi^{(7)}(0+0)=1$.

Let us first demonstrate the adverse effect that we would subsequently like to counter. The geometry of the computation is shown in Fig. 2, the width of the PML is set to $l=1$, and the magnitude of damping $\sigma_0=10$, see formula (22). The PML is terminated with the characteristic boundary conditions (24).

In Fig. 4, we are showing the profiles of the error (its binary logarithm) for the magnetic field H_θ evaluated on the domain Ω in the maximum (i.e., L_∞) norm. The solutions are computed on the sequence of four square cell grids with sizes $h=0.1, 0.05, 0.025$, and 0.0125. The H_θ error at every grid node is defined as the difference between the numerical solution and the exact solution (36c). The computations are run until $t=400$, which is about 40 times the time required for the waves to cross the computational domain Ω.

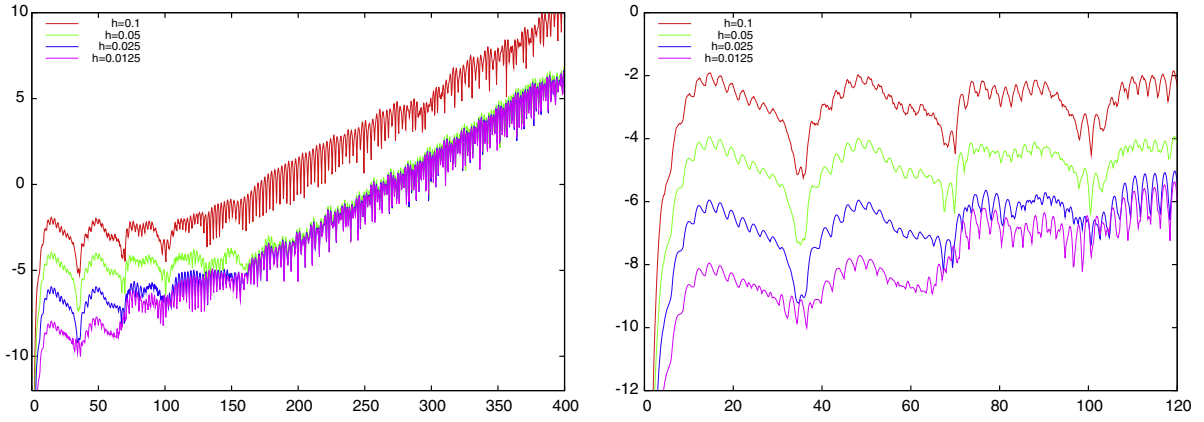

Fig. 4. Computation with the PML (21). Binary logarithm of the maximum norm error for H_θ vs. time.

Some immediate observations from Fig. 4 are as follows. At the initial stage of computation the numerical solution demonstrates the design rate of grid convergence — $\mathcal{O}(h^2)$; this is most clearly seen on the zoomed-in plot of Fig. 4b. At later stages, however, the error starts to increase, and the solution deteriorates, see Fig. 4a. The rate of deterioration is pretty much the same for all grids, however, the onset occurs somewhat earlier on finer grids.

In Fig. 5, we are showing two plots similar to those from Fig. 4. The computational setup that corresponds to Fig. 5 is identical to that behind Fig. 4 with one major exception — the PML is switched off, i.e., $\sigma(z) \equiv 0$. We see that the behavior of the error curves shown in Fig. 5 differs from that of Fig. 4 in two key aspects. On one hand, the grid convergence gets saturated rather early, there is practically no difference in the absolute value of the error already between $h = 0.05$ and $h = 0.025$. The explanation is straightforward — the error inside Ω is dominated by the reflections from the boundaries $z = 5 + l$ and $z = -5 - l$, see Fig. 2, and the magnitude of those reflections is not related to the grid size. In other words, the characteristic boundary conditions (24) only allow to get so far down in error. On the other hand, we see that in Fig. 5 there is no long-time error growth of the type Fig. 4 shows. As the PML is the only difference between the two setups, we conclude that the deterioration of the numerical solution observed in Fig. 4 should unambiguously be attributed to the presence of the PML.

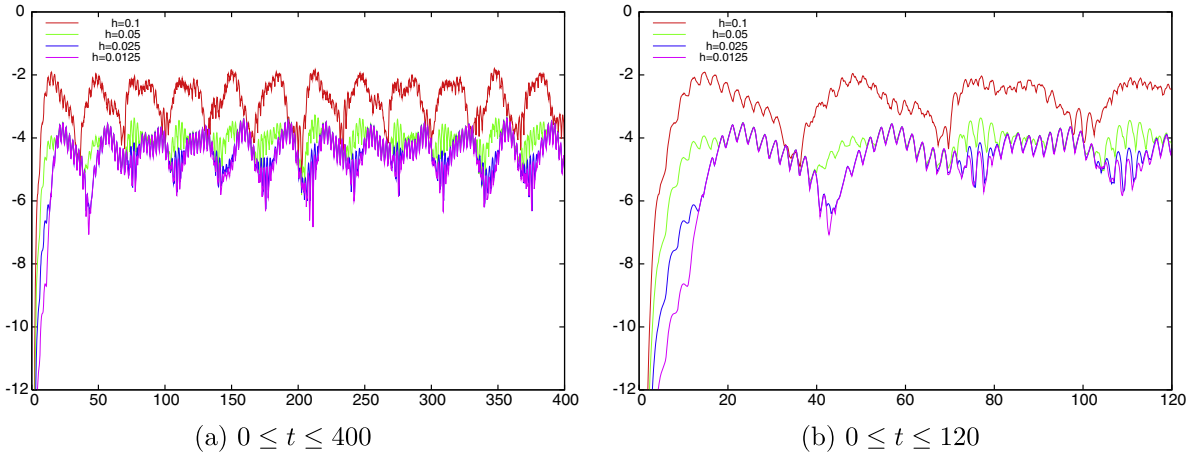

Fig. 5. Computation with the characteristic boundary conditions (24) only. Binary logarithm of the maximum norm error for H_θ vs. time.

To avoid any potential inaccuracies in the foregoing comparison, in Fig. 6 we are showing the same error profiles as in Fig. 4a and Fig. 5a, but grouped according to the grid. This allows us to present the PML and no-PML error curves for every grid right next to one another in precisely the same scale. We conclude that on the coarsest grid $h = 0.1$, see Fig. 6a, the overall error is dominated by that of the interior discretization, because the two curves coincide in the beginning and at a later stage the PML solution deteriorates. On finer grids, see Figs. 6b–d, the accuracy of the PML solution at the initial stage improves as the grid size decreases, but then the long-time instability kicks in. At the same time, the error curves for the characteristic boundary conditions remain "flat" for all t, but the accuracy does not improve as the grid is refined because of the reflections from the outer boundary.

Several comments are in order before we proceed to describing the results of computations with the lacunae-based method of Section 2.

- The error profiles for E_r and E_z in all the cases (including those with lacunae) look very much like those for H_θ, and we do not present them hereafter.
- We have repeated the PML computations with the layer twice as thick, $l = 2$, and the results were practically indistinguishable from those shown in Fig. 4. Hence, we conclude that already with $l = 1$ the layer provides enough damping so that the error on Ω is dominated by that of the interior discretization. We later corroborate this conclusion by the computations with genuine lacunae-based termination as in [29].

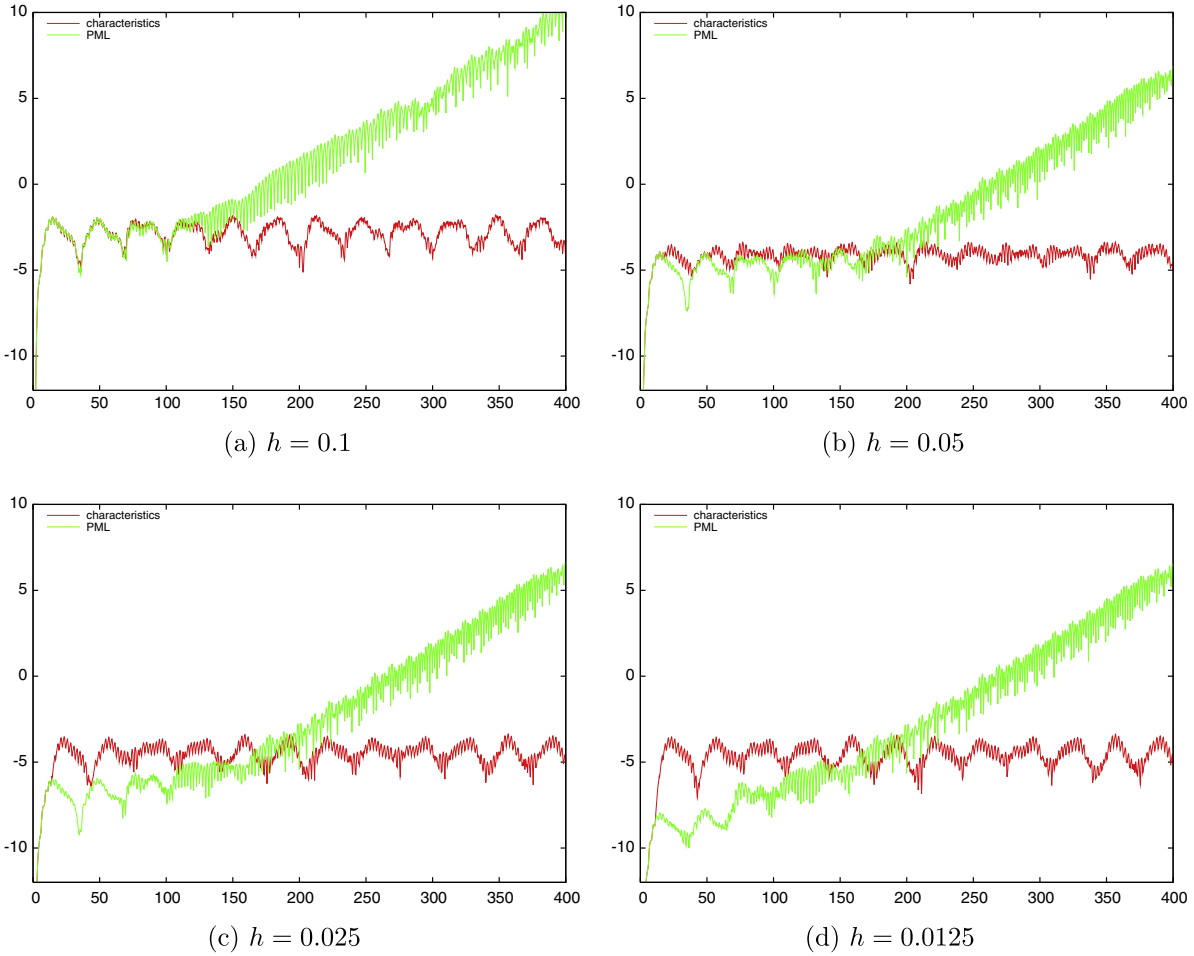

Fig. 6. Comparison of the case with the PML against that with no PML on four grids. Binary logarithm of the maximum norm error for H_θ vs. time.

- We have also repeated the PML computations while terminating the layer with the zero Dirichlet boundary conditions rather than the characteristic boundary conditions (24). Again, the results were practically indistinguishable from those shown in Fig. 4. Hence, we conclude that as long as the layer provides enough damping, the outer boundary condition does not make much of a difference.
- The increase of σ_0 does not make any difference in the results either.
- Finally, the log-linear curves shown in Fig. 4a indicate that as the computation advances, the error increases with a slow yet exponential rate. At the same time, the continuous analysis of [15] predicts a polynomial growth. On one hand, we note in this regard that the problem analyzed in [15] was driven only by the initial conditions and had zero RHS, whereas in this paper the solution is driven by a continuously operating source. On the other hand, the polynomial growth was predicted in [15] for a continuous formulation based on the presence of multiple eigenvalues in the amplification matrix. At the same time, we have seen in [16] that sometimes a multiple eigenvalue may get split by the discretization yet the growth will stay while in some other cases a multiple continuous eigenvalue will remain multiple for the discretization yet there will be no growth. Consequently, we can say that the reasons for the long-term deterioration of solution in the PML may not be fully understood yet, and there is apparently room for the growth faster than polynomial. (The observed growth is not a numerical instability, because it is not faster on finer grids.) However, as mentioned in Sections 1 and 2, and as subsequent computations clearly show, the lacunae-based integration allows to correct the long-time growth regardless of its origins and its specific rate (as long as the latter is not catastrophically fast).

Let us now demonstrate how the lacunae-based integration is combined with the PML (21). For the parameters of the partition, we take $T_0 = 44$ and $\Delta T = 2$, see Fig. 3. In Fig. 7, we are showing the results of computations for exactly the same setup as the one behind Fig. 4, but with the lacunae-based correction applied (the vertical scale on Fig. 4a and Fig. 7a is not the same). We see that the long-time growth completely disappears due to the lacunae-based correction, and the numerical solution shows the design second order grid convergence for the entire duration of the integration interval.

As before, to avoid any potential inaccuracies in the foregoing comparison, say, due to different scales on different plots, in Fig. 8 we are showing the same error profiles as in Figs. 4a and 7a, but grouped according to the grid. This allows us to present the pure PML error profiles and the PML + lacunae profiles for every grid right next to one another in precisely the same scale. We see that at the initial stage the two error curves coincide on every grid, and the actual values of the error are decreasing with the design rate as the grid is refined. Later, the pure PML solutions completely lose their accuracy, whereas the solutions with the lacunae-based correction can maintain it for as long as the computation is run.

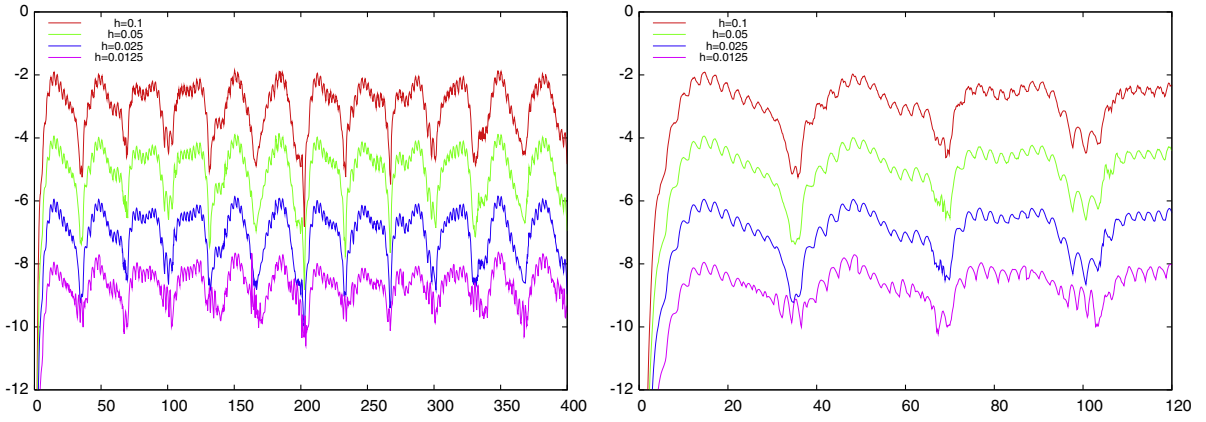

(a) $0 \le t \le 400$ (b) $0 \le t \le 120$

Fig. 7. Computation with the PML (21) and lacunae-based correction. Binary logarithm of the maximum norm error for H_θ vs. time.

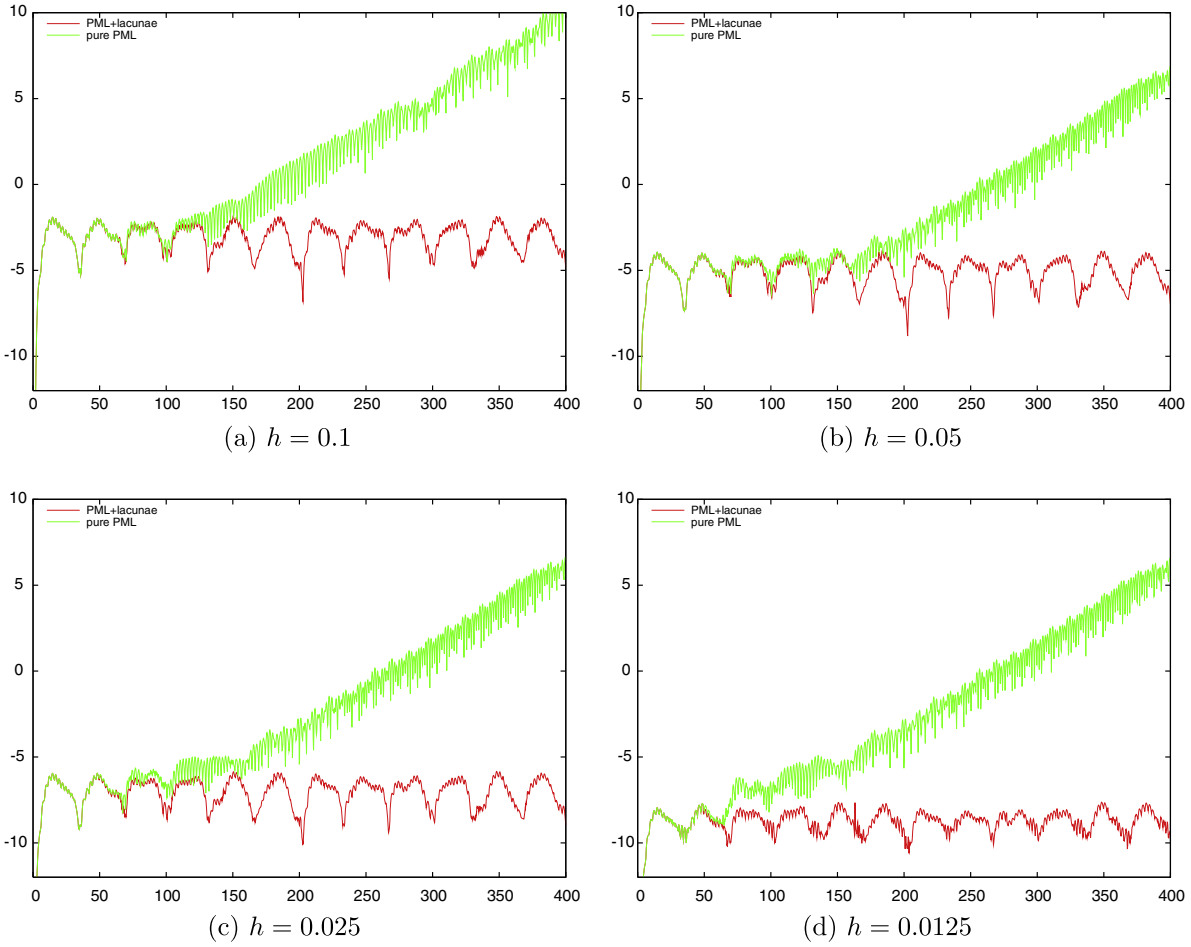

Fig. 8. Comparison of the pure PML case against that with the PML and lacunae on four grids. Binary logarithm of the maximum norm error for H_0 vs. time.

We note that the computational overhead associated with the application of lacunae-based algorithm along with the PML is not overwhelming. According to formula (40), the fraction of the overall time when we need to compute two solutions is $(T + \Delta T)/(t_{m+1} - t_m)$, and the rest of the time we compute only one solution. For the domain Ω shown in Fig. 2, we have $T \approx 11$ (recall, $c = 1$), and with $T_0 = 44$ and $\Delta T = 2$ we can write:

$$\frac{T + \Delta T}{t_{m+1} - t_m} \equiv \frac{T + \Delta T}{T_1} \approx 0.31,$$

which puts the overhead at approximately 31%. The same series of computations with the PML and lacunae-based correction was, in fact, repeated for $T_0 = 64$ and $\Delta T = 2$. The results were very similar to those shown in Figs. 7 and 8, with the overhead of about 21%.

The only question that still needs to be addressed is that of the "optimality" of the proposed lacunae + PML treatment of the boundaries. In other words, whether or not a different approach can offer an even better overall accuracy compared to what Figs. 7 and 8 show. To look into this issue, we compare the results obtained using the combination of lacunae and the PML with those obtained using the pure lacunae-based termination of the computational domain [29]. The original method of [29] requires buffer zones to surround Ω wider than the PML, and consequently, the computations are more expensive. However, the method of [29] *provably introduces no error associated with the domain truncation.* Hence, the only source of the error on Ω is the interior discretization. In Fig. 9, we compare the error profiles for the pure lacunae case and for the lacunae + PML case on four grids.

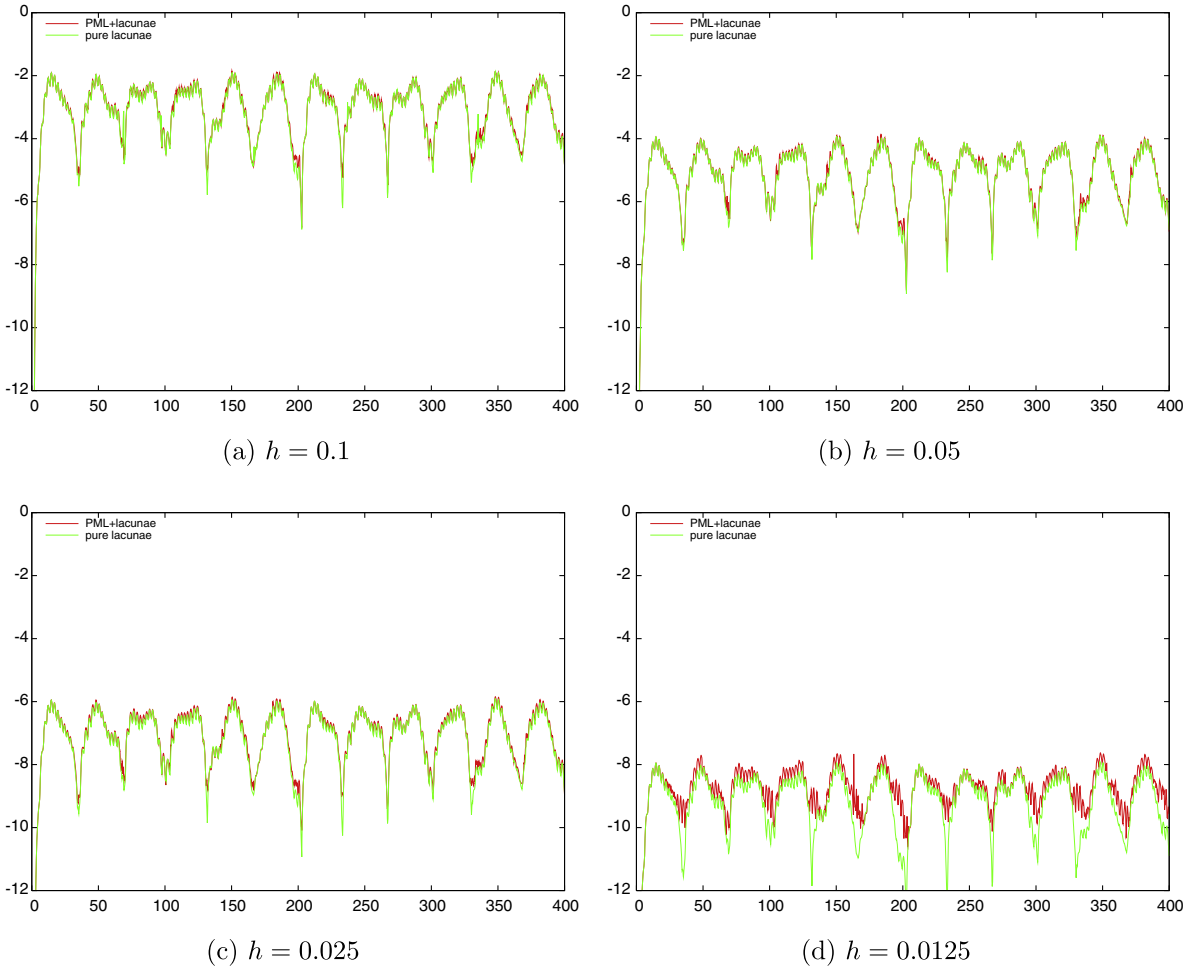

Fig. 9. Comparison of the pure lacunae case against that with the PML and lacunae on four grids. Binary logarithm of the maximum norm error for H_θ vs. time.

We see that the two curves basically sit on top of one another for every grid. Hence, the error on Ω obtained using the combined lacunae + PML methodology is the same as that for the pure lacunae-based approach. As the latter is due to the interior discretization only, we conclude that the accuracy of the boundary treatment offered by the combined lacunae + PML methodology exceeds the accuracy of the scheme on Ω and consequently, the overall accuracy cannot be further improved by changing the boundary procedure.

4. Extensions

In this section, we review the application of lacunae-based methods to setting the ABCs [31–33], and show that the same approach will allow us to extend the applicability of the proposed lacunae-based stabilization of PMLs well beyond the simple problems of radiation of waves by known sources. The following problem formulation that requires unsteady ABCs is typical for many applications. The wave field of interest is generated inside the bounded domain $\Omega \subset \mathbb{R}^3$ and further propagates outward. We assume that in *the far field,* i.e., on the complementary domain $\mathbb{R}^3 \setminus \Omega$, the propagation of waves is governed by the linear homogeneous system [cf. formula (1)]:

$$\frac{\partial \boldsymbol{w}}{\partial t} + \boldsymbol{L}\boldsymbol{w} = \boldsymbol{0}, \quad \boldsymbol{x} \in \mathbb{R}^3 \setminus \Omega, \quad t > 0. \tag{42}$$

For our analysis we need to assume that Eq. (42) is Huygens'. The waves' generation mechanism inside Ω can be sophisticated. It can include actual sources (antennas), scatterers, and other objects, there can be damping, the waves can undergo multiple scattering, etc. Moreover, the model inside Ω does not have to be Huygens'. *Our key assumption, however, is that the overall problem solved both inside and outside Ω has a unique solution.* The goal is to be able to actually solve this problem only in *the near field,* i.e., on Ω, while truncating all of its exterior and replacing it with the appropriate closure procedure at the external boundary $\partial\Omega$, e.g., the ABCs or PML. The assumption on the overall unique solvability will allow us to focus independently on the design of the closure, i.e., on the proper treatment of the outgoing waves.

The first step is the decomposition of the original problem into the interior and auxiliary subproblems. The interior problem is formulated on the bounded domain Ω, it is obtained by truncating the original formulation and as such, it inherits all the features of the latter. It is the interior problem that requires a closure at $\partial\Omega$. The auxiliary problem is formulated on the entire space $\mathbb{R}^3$. This problem is of the type (1), with the homogeneous initial conditions: $\boldsymbol{\varphi} = \boldsymbol{0}$. Its solution is driven by the specially constructed auxiliary source terms $\boldsymbol{f}(\boldsymbol{x}, t)$ that are compactly supported in space for all times on a narrow region $\Omega \setminus \Omega_\varepsilon$ next to the boundary $\partial\Omega$, see Fig. 10. All the sophisticated features of the interior problem (such as scatterers) are supposed to be confined to Ω_ε.

The two problems are connected to one another. The auxiliary sources depend on the interior solution right inside Ω, and the solution of the auxiliary problem right outside Ω can provide the missing data and thus enable a closure for the interior formulation. The construction of the auxiliary sources is described in [31–33]. *It guarantees equivalence* between the original problem before the decomposition and the two subproblems after the decomposition considered together. This means, in particular, that the solution of the auxiliary problem on $\mathbb{R}^3 \setminus \Omega$, i.e., the outgoing field, coincides with the solution of the original problem. The key benefit from employing the decomposition is that by design, the auxiliary problem satisfies the Huygens' principle. The unsteady ABCs of [31–33] are obtained by solving the auxiliary problem with the help of lacunae and supplying the missing boundary data to the interior problem.

We emphasize that although the auxiliary sources depend on the interior solution, it does not imply that the interior problem requires a separate algorithm to be solved. Likewise, the fact that the closure for the interior problem is provided by the exterior solution does not imply that the auxiliary problem has to be solved on the extended region far away from Ω. In fact, both problems are time marched synchronously. Once the interior solution is advanced one time step, the auxiliary sources can also be advanced one time step. Then, the exterior solution can be obtained on the next level; it needs to be known only right outside Ω. This solution provides the missing closure for the interior problem on the upper time level, after which the interior solution can be advanced yet one more step, and the procedure cyclically repeats itself. We refer the reader to [31–33] for additional detail on lacunae-based ABCs.

The exact same idea of decomposition can be applied in the framework of stabilizing the PMLs. The PML that surrounds Ω, see Fig. 1, is designed to absorb all the outgoing waves. The outgoing waves are the same

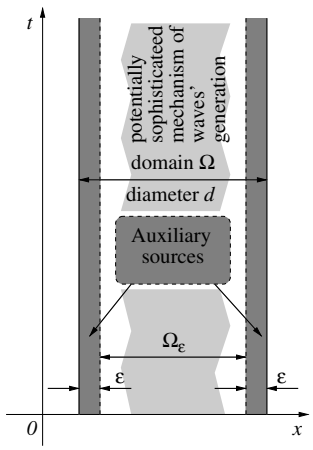

Fig. 10. Decomposition of the problem.

whether they are due to the original radiation/scattering mechanism on Ω_ε or to the auxiliary sources on $\Omega \setminus \Omega_\varepsilon$, see Fig. 10. Hence, the lacunae-based methodology of Section 2 can be applied to the auxiliary problem, which will enable stabilization of the PML without having to put any restrictions on the model inside Ω_ε (besides the requirement of the overall unique solvability).

5. Discussion

In Section 2, we have proved theoretically, and in Section 3 shown experimentally, that lacunae-based integration indeed provides an efficient tool for removing the long-term instabilities induced by PMLs. In doing so, the numerical error becomes uniformly bounded in time.

There is actually no contradiction in obtaining temporally uniform error bounds for the problem that is only weakly well-posed. The explanation is that the lacunae-based algorithm alters the solution of the combined problem inside the PML, and the overall solution coincides with the solution of (1) only on the domain Ω, where the Huygens' principle holds. At the same time, unlike in [15], the PML equations never get modified by lacunae-based integration, and for each problem (12) the layer remains perfectly matched and absorbing.

It is also clear that even though we have only considered the perturbations of the initial data $\boldsymbol{\xi}$ in Section 2, we would have obtained similar temporally uniform estimates if the perturbations of the RHS were included as well. The computations of Section 3 corroborate this conclusion experimentally.

The analysis of Section 2 imposes *no constraints on the rate of growth* $\mu(t)$, see (10), and C_0 in inequality (15b) is a constant in any event. The actual value of this constant $C_0 = \mu(T_1 + T) \cdot (M - M_0 + 1)$, however, may or may not be acceptable in a particular context. If $\mu(t)$ is a slowly increasing function, such as a low degree polynomial, then C_0 will not be large. In Section 3.4 we saw that the PML-induced growth may, in fact, be non-uniform. At the initial stage, there was no growth at all, and after that it would pick up. Hence, we chose the parameters in such a way so that to keep $T_1 + T$ within the range of no growth and consequently have a low value of $\mu(T_1 + T)$.

It is also important to emphasize that *the source of the growth inside the PML does not matter either*. It can be the mechanism identified in [15], but by no means does it have to be this mechanism only. For example, if *the corner in the PML* leads to long-term instabilities, the lacunae-based methodology will address those as well. In fact, since the idea of the lacunae-based methodology that we have introduced is to represent the solution that evolves over long times as the sum of a finite number of components that each has a finite fixed "lifespan," the methodology can be used for alleviating any other undesirable long-term phenomenon in computation.

Note, however, that while the proposed procedure alleviates the growth of the field inside the PML, *it does not offer a fix for the numerical instability*. In other words, if the error estimate for the scheme deteriorates as the grid is refined, the deterioration will be inherited by the discretization of every problem (12). If, however, the deterioration rate is slow (e.g., linear as in [6]), then the overall algorithm may still be viable.

The computational overhead of the proposed procedure is $\sim (T + \Delta T)/T_1$, which can be kept at acceptable levels by choosing sufficiently large $T_1 = T_0 - \Delta T$. Specific values should be determined by actual numerical experiments.

In Section 2, we have only considered a PML of infinite thickness, whereas in real implementations, such as that of Section 3, the thickness is always finite. Termination of the PML at a finite distance results in reflections from the outer boundary that propagate back through the layer and then re-enter the computational domain. If, however, the damping inside the PML is sufficiently strong, the magnitude of these reflections is small. Hence, even though the lacunae-based algorithm won't help remove or reduce those reflections, the accuracy of the combined PML + lacunae boundary procedure can still be made sufficiently high so that to have the overall accuracy inside the computational domain dominated by that of the interior discretization (Section 3.4).

For Maxwell's equations, there is a necessary solvability condition given by the continuity equation for currents and charges (Eq. (18) in the cylindrically symmetric TE case). Partition of the RHS (38) may break the continuity, that's why for the numerical tests of Section 3 we have chosen zero charges and solenoidal currents (37a), (37b) that satisfy the continuity equation identically. As far as the more general framework outlined in Section 4, it has been shown in [33] that the auxiliary sources on $\Omega \setminus \Omega_\varepsilon$, see Fig. 10, can also be obtained in the

form of solenoidal currents and zero charges. Hence, they can withstand partition (38) with no violation of continuity.

Finally, the original problem (1) was formulated for a first order system, and numerical simulations of Section 3 have also been conducted using the first order system (16) as an example. Instead, we could have had a second order equation or system in (1), e.g., the d'Alembert equation itself. Note, there are examples of systems, as opposed to scalar equations, that do not reduce to the d'Alembert equation and yet are Huygens'.[5]

Acknowledgment

Research supported by the US Air Force, Grants Nos. FA9550-04-1-0118 and FA9550-07-1-0170, and US NSF, Grant No. DMS-0509695.

References

[1] T. Hagstrom, Radiation boundary conditions for the numerical simulation of waves, in: Acta Numerica, 1999, vol. 8 of Acta Numer., Cambridge University Press, Cambridge, 1999, pp. 47–106.
[2] S.V. Tsynkov, Numerical solution of problems on unbounded domains. A review, Appl. Numer. Math. 27 (1998) 465–532.
[3] J.-P. Bérenger, A perfectly matched layer for the absorption of electromagnetic waves, J. Comput. Phys. 114 (2) (1994) 185–200.
[4] J.-P. Bérenger, Three-dimensional perfectly matched layer for the absorption of electromagnetic waves, J. Comput. Phys. 127 (2) (1996) 363–379.
[5] F.Q. Hu, On absorbing boundary conditions for linearized Euler equations by a perfectly matched layer, J. Comput. Phys. 129 (1) (1996) 201–219.
[6] S. Abarbanel, D. Gottlieb, A mathematical analysis of the PML method, J. Comput. Phys. 134 (2) (1997) 357–363.
[7] H.-O. Kreiss, J. Lorenz, Initial-Boundary Value Problems and the Navier–Stokes Equations, Pure and Applied Mathematics, Academic Press Inc., Boston, MA, 1989, vol. 136.
[8] S.A. Cummer, A simple, nearly perfectly matched layer for general electromagnetic media, IEEE Microwave Wireless Components Lett. 13 (3) (2003) 128–130.
[9] E. Bécache, P. Joly, On the analysis of Bérenger's perfectly matched layers for Maxwell's equations, M2AN Math. Model. Numer. Anal. 36 (1) (2002) 87–119.
[10] K.S. Yee, Numerical solution of initial boundary value problem involving Maxwell's equations in isotropic media, IEEE Trans. Antennas Propagat. 14 (1966) 302–307.
[11] S.D. Gedney, An anisotropic perfectly matched layer-absorbing medium for the truncation of FDTD lattices, IEEE Trans. Antennas Propagat. 44 (12) (1996) 1630–1639.
[12] R.W. Ziolkowski, Time-derivative Lorenz material model based absorbing boundary conditions, IEEE Trans. Antennas Propagat. 45 (10) (1997) 1530–1535.
[13] S. Abarbanel, D. Gottlieb, On the construction and analysis of absorbing layers in CEM, Appl. Numer. Math. 27 (4) (1998) 331–340.
[14] J.S. Hesthaven, On the analysis and construction of perfectly matched layers for the linearized Euler equations, J. Comput. Phys. 142 (1) (1998) 129–147.
[15] S. Abarbanel, D. Gottlieb, J.S. Hesthaven, Long time behavior of the perfectly matched layer equations in computational electromagnetics, J. Sci. Comput. 17 (1-4) (2002) 405–422.
[16] S. Abarbanel, H. Qasimov, S. Tsynkov, Long-time performance of unsplit PMLs with explicit second order schemes, J. Sci. Comput. (submitted for publication).
[17] E. Bécache, P.G. Petropoulos, S.D. Gedney, On the long-time behavior of unsplit perfectly matched layers, IEEE Trans. Antennas Propagat. 52 (5) (2004) 1335–1342.
[18] F.L. Teixeira, W.C. Chew, Finite-difference computation of transient electromagnetic waves for cylindrical geometries in complex media, IEEE Trans. Geosci. Remote Sensing 38 (4) (2000) 1530–1543.
[19] S. Abarbanel, D. Gottlieb, J.S. Hesthaven, Non-linear PML equations for time dependent electromagnetics in three dimensions, J. Sci. Comput. 28 (2-3) (2006) 125–137.
[20] S.D. Gedney, The perfectly matched layer absorbing medium, in: A. Taflove (Ed.), Advances in Computational Electrodynamics: The Finite-Difference Time-Domain Method, Artech House, Boston, MA, 1998, pp. 263–340.
[21] J.A. Roden, S.D. Gedney, Convolution PML(CPML): an efficient FDTD implementation of the CFS-PML for arbitrary media, Microwave Opt. Technol. Lett. 27 (5) (2000) 334–339.
[22] P.G. Petropoulos, Reflectionless sponge layers as absorbing boundary conditions for the numerical solution of Maxwell equations in rectangular cylindrical and spherical coordinates, SIAM J. Appl. Math. 60 (3) (2000) 1037–1058.
[23] J. Hadamard, Lectures on Cauchy's Problem in Linear Partial Differential Equations, Yale University Press, New Haven, 1923.
[24] J. Hadamard, Problème de Cauchy, Hermann et cie, Paris, 1932 [French].

[5] Because systems are not covered by the result of [35].

[25] J. Hadamard, The problem of diffusion of waves, Ann. Math. (2 4) (1942) 510–522.
[26] R. Courant, D. Hilbert, Methods of Mathematical Physics, vol. 2, Wiley, New York, 1962.
[27] M. Belger, R. Schimming, V. Wünsch, A survey on Huygens' principle, Z. Anal. Anwendungen 16 (1) (1997) 9–36, dedicated to the memory of Paul Günther.
[28] P. Günther, Huygens' Principle and Hyperbolic Equations, Vol. 5 of Perspectives in Mathematics, Academic Press Inc., Boston, MA, 1988 (with appendices by V. Wünsch).
[29] V.S. Ryaben'kii, S.V. Tsynkov, V.I. Turchaninov, Long-time numerical computation of wave-type solutions driven by moving sources, Appl. Numer. Math. 38 (2001) 187–222.
[30] I. Petrowsky, On the diffusion of waves and the lacunas for hyperbolic equations, Matematicheskii Sbornik (Recueil Mathématique) 17 (59 3) (1945) 289–370.
[31] V.S. Ryaben'kii, S.V. Tsynkov, V.I. Turchaninov, Global discrete artificial boundary conditions for time-dependent wave propagation, J. Comput. Phys. 174 (2) (2001) 712–758.
[32] S.V. Tsynkov, Artificial boundary conditions for the numerical simulation of unsteady acoustic waves, J. Comput. Phys. 189 (2) (2003) 626–650.
[33] S.V. Tsynkov, On the application of lacunae-based methods to Maxwell's equations, J. Comput. Phys. 199 (1) (2004) 126–149.
[34] F.L. Teixeira, W.C. Chew, PML-FDTD in cylindrical and spherical grids, IEEE Microwave Guided Wave Lett. 7 (9) (1997) 285–287.
[35] M. Matthisson, Le probléme de Hadamard relatif á la diffusion des ondes, Acta Math. 71 (1939) 249–282 [French].
[36] A. Bayliss, E. Turkel, Radiation boundary conditions for wave-like equations, Comm. Pure Appl. Math. 33 (6) (1980) 707–725.
[37] A. Bayliss, E. Turkel, Outflow boundary conditions for fluid dynamics, SIAM J. Sci. Statist. Comput. 3 (2) (1982) 250–259.
[38] A. Bayliss, E. Turkel, Far field boundary conditions for compressible flows, J. Comput. Phys. 48 (2) (1982) 182–199.
[39] A. Bayliss, M. Gunzburger, E. Turkel, Boundary conditions for the numerical solution of elliptic equations in exterior regions, SIAM J. Appl. Math. 42 (2) (1982) 430–451.
[40] V.S. Ryaben'kii, S.V. Tsynkov, A Theoretical Introduction to Numerical Analysis, Chapman & Hall/CRC, Boca Raton, FL, 2007.
[41] L.D. Landau, E.M. Lifshitz, Course of Theoretical Physics, vol. 2, The Classical Theory of Fields, fourth ed., Pergamon Press, Oxford, 1975, translated from the Russian by Morton Hamermesh.